Highlights

A Bayesian CAIPIVAT Approach with Through-Plane Acceleration to Enhance Efficiency of Simultaneously Encoded Slice Acquisition in FMRI

Ke Xu, Daniel B. Rowe

- Traditional fMRI image reconstruction is both costly and time-consuming

- The SMS technique boosts the efficiency of the image acquisition process

- The mSPECS-CAIPIVAT technique reduces overlap between aliased slices

A Bayesian CAIPIVAT Approach with Through-Plane Acceleration to Enhance Efficiency of Simultaneously Encoded Slice Acquisition in FMRI

Ke Xu[a], Daniel B. Rowe[a]

[a]*Computational Mathematical and Statistical Sciences Department, Marquette University, 1313 W. Wisconsin Ave, Milwaukee, 53233, WI, USA*

Abstract

FMRI has been a safe medical imaging tool to study brain function by demonstrating the spatial and temporal changes in brain metabolism in recent decades. To capture brain functionality more efficiently, efforts have been made to accelerate the number of images acquired per unit of time that create each volume image without losing full anatomical structure. The Simultaneous Multi-Slice (SMS) technique provides a reconstruction method where multiple slices are acquired and aliased concurrently. Traditional imaging techniques such as SENSE and GRAPPA can reconstruct an image from less measured data but have their drawbacks. The Controlled Aliasing in Parallel Imaging (CAIPI) and view angle tilting (VAT) technique achieves slice-wise image shift to decrease the influence of the geometry factor (g-factor) of coil sensitivities and prevents the singular problem of the design matrix. In this paper, a Bayesian CAIPIVAT approach for multi-coil separation of parallel encoded complex-valued slices (mSPECS-CAIPIVAT), a novel SMS approach is presented, combined with the Hadamard phase-encoding method. Our proposed approach was applied to simulation and experimental study showing a decrease in the influence of the g-factor while increasing the brain activation detection rate. The signal-to-noise ratio and the contrast-to-noise ratio are also improved by our approach.

Keywords:
fMRI, SMS, Through-Plane, CAIPIVAT

1. Introduction

As a powerful and non-invasive medical imaging tool, functional Magnetic Resonance Imaging (fMRI) has played a dominant role in brain imaging studies since 1990 (Ogawa et al. (1990)). The activity of neurons cannot be directly detected but is correlated to the Blood Oxygen Level Dependence (BOLD) contrast signal which is used as a proxy. By detecting task-related changes in the BOLD signal inside our brain, the magnetic resonance (MR) scanner can map our brain with a unique radio frequency (RF) pulse sequence (Ogawa et al. (1990); Glover (2011)). The Gradient Echo Echo-Planer Imaging (GE-EPI) pulse sequence is widely used in fMRI studies to shorten the scan time and decrease the influence of the motion of subjects by acquiring full k-space spatial information within a single excitation (Mansfield (1977); Rzedzian et al. (1983); Piustchi-Amin et al. (2001)). In structural and functional MRI studies, the time to measure a volume image is dependent upon how rapidly the amount of data necessary to reconstruct an image can be measured. In order to accelerate the number of images measured per unit time, a topic of study has been to measure less data but still be able to reconstruct a high-quality image. To reconstruct images using less data, multiple receiver coils are used where each coil measures sensitivity-weighted images (Hyde et al. (1986)). Initially, accelerated imaging was aimed at In-Plane Acceleration (IPA) where spatial frequency data are partially skipped, and each coil measured fewer lines of spatial frequency. In parallel imaging techniques, like Sensitivity Encoding (SENSE) and Generalized Autocalibrating Partially Parallel Acquisitions (GRAPPA) (Pruessmnn et al. (1999); Griswold et al. (2002)), a single slice has been excited, and partial lines of k-space skipped, resulting in a sensitivity weighted aliased image for each coil, that is combined into a single complete image. Bayesian techniques have been applied to improve the resolution of the reconstructed images by incorporating the anatomical information from prior distribution into the k-space (Kornak et al. (2010)). Other in-plane imaging acceleration techniques like partial Fourier imaging technique (Feinberg et al. (1986); Noll et al. (1991)) can acquire half of the lines in the k-space. The unacquired frequency data can be determined due to the Hermitian symmetry property of the k-space to reconstruct real-valued images. Moreover, a rapid three dimensional volume-image method has been established to sample the k-space (Lindquist et al. (2008)). However, considering some fixed time blocks in the data-acquiring process, for instance, imaging encoding and the proper time for T_2^* contrast in one
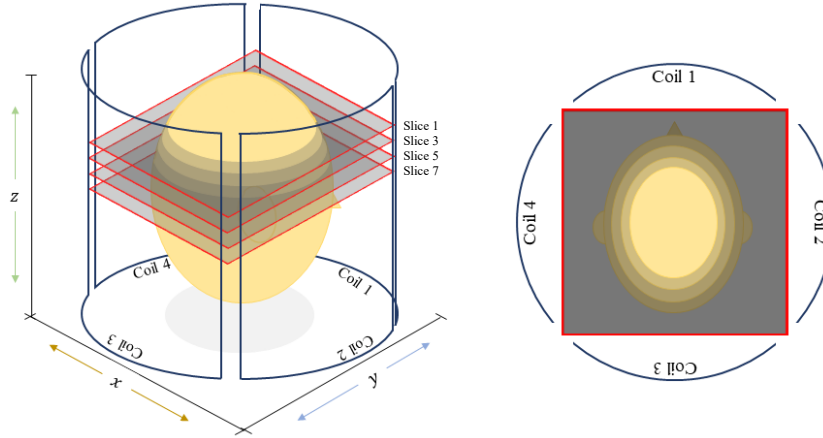
Figure 1: The 3D view (left) and 2D view (right) of an example for SMS technique with four slices and four coils.

excitation, the scan time will not decrease significantly in IPA techniques. More recently, Simultaneous Multi-Slice (SMS) techniques (Figure. 1) were developed and discussed (Souza et al. (1988); Rowe et al. (2013); Barth et al. (2016)). The SMS technique is extensively used in fMRI studies, and it allows for acquiring fMRI data with high resolution by using a multiband (MB) radiofrequency (RF) within a reduced repetition time (TR). Compared with conventional parallel imaging techniques, in SMS techniques, multiple slices are acquired concurrently and aliased together in one excitation, and hence, the image-acquiring time will decrease with a factor of the total number of aliased slices. Thus, a Through-Plane Acceleration (TPA) is achieved by SMS techniques and allows for a more efficient approach to acquiring images. In this paper, a novel SMS imaging reconstruction technique with high acceleration factor, a Bayesian Controlled Aliasing in Parallel Imaging with View Angle Tilting approach for multi-coil Separation of Parallel Encoded Complex-valued Slices (mSPECS-CAIPIVAT), will be presented and discussed.

Since multiple slices are acquired at the same time for one excitation of the TPA technique, a short distance between aliased slices will lead to a high similarity of voxel and coil sensitivity information. When applying the standard SENSE method, this may cause a singular matrix problem and strong inter-slice signal leakage will appear on the reconstructed images. To decrease the influence of the geometry properties of the coil sensitivity maps, techniques

like "controlled aliasing in parallel imaging results in higher acceleration" (CAIPIRINHA), "blipped-CAIPIRINHA" (Blipped-CAIPI), and Hadamard phase-encoding provide other possible ways to minimize the influence of the geometric factor (g-factor) and increase the conditioning of the slices aliasing matrix (Breuer et al. (2005); Setsompop et al. (2012)). By modulating the phase for each line in k-space and imparting each line with a specific angle, the field-of-view (FOV) will be moved in the phase encoding direction (PE, vertically in this paper). Applying a unique phase modulation amount to each slice in the aliased image-acquiring process increases the physical distance between the aliased voxels. Therefore, the difference of coil sensitivity for each slice will increase and the influence of the g-factor for each excitation will be minimized. Moreover, to further increase the physical distance between two aliased voxels and expose more information beneath the coil sensitivities, the FOV can not only be moved along the vertical PE direction but also the horizontal readout direction (RO, horizontally in this paper). The study "multislice CAPIPRINHA using view angle tilting technique" (CAIPIVAT) (Jungmann et al. (2015); Kim et al. (2016)) proposes a method combining the CAIPIRINHA technique and View Angle Tilting (VAT) (Kim et al. (2012)) technique together by applying a unique compensation gradient of VAT. Other techniques to solve the singular matrix problem of the design matrix, like the "simultaneous multi-slice acquisition" (SIMA) (Souza et al. (1988)) method discussed a powerful tool, the Hadamard phased-encoding technique in the reconstruction process. By incorporating a specific coefficient from the Hadamard matrix for each aliasing slice, different combinations for each voxel will be achieved. For example, the summation of two desired voxels will not only be acquired but also the difference between two voxels will be collected. Moreover, the Hadamard phase-encoding technique has been proved to be a significant method to minimize the residual correlation between the unaliased images and improve the temporal signal-to-noise ratio ($tSNR$) (Nencka (2013); Nencka (2013)). In the "Separation of parallel encoded complex-valued slices (SPECS) from a single complex-valued aliased coil image" and "multi-coil separation of parallel encoded complex-valued slices" (mSPECS) studies, the Hadamard phase encoding technique is also the essential idea (Rowe et al. (2016); Kociuba (2016)). The SPECS technique and the mSPECS technique are critical milestones of this study.

In our mSPECS-CAIPIVAT model, we incorporate slice-wise image shift techniques and the Hadamard phase-encoding technique together in which different voxel combinations will be acquired for each excitation. In the
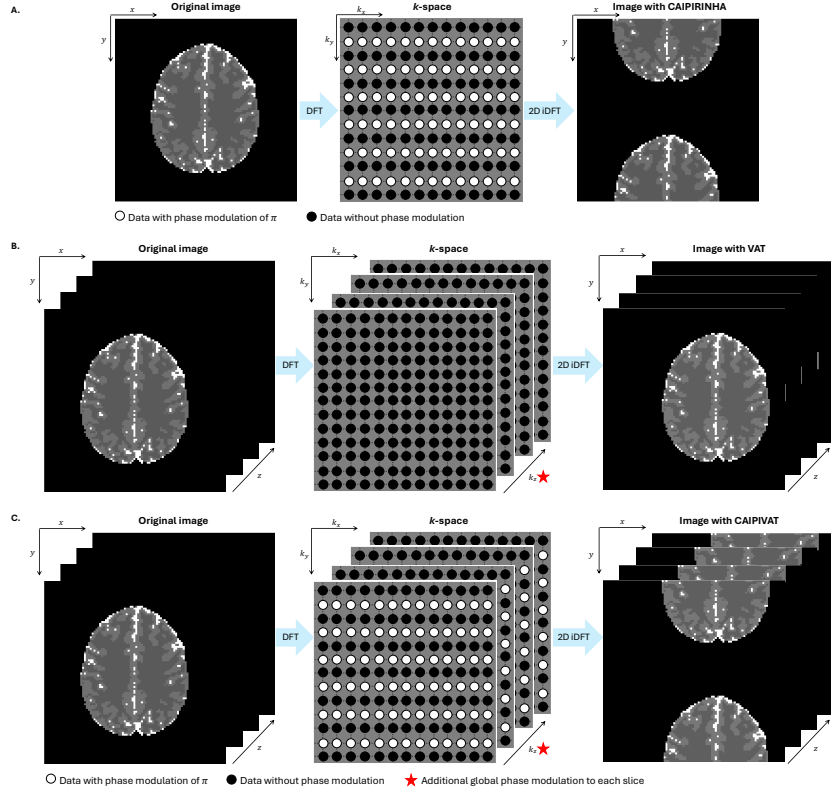
Figure 2: A. An illustration of the CAIPIRINHA process. B. An illustration of the VAT process. C. An illustration of the CAIPIVAT process.

unaliasing process, calibration reference images will be artificially aliased, and the artificial aliasing matrix will be used to assess hyperparameters of prior distribution in the separation process. The artificial aliased calibration imaging technique and bootstrap sampling approach is combined and applied into the model to eliminate the inter-slice signal leakage in the reconstruction images at the cost of a slightly increased variance of the calibration images forming the prior variance. The maximum a posteriori technique is applied in this model to calculate the estimated reconstruction voxel values. The mSPECS-CAIPIVAT model provides a solution to significantly reduce the scan time with a high acceleration factor, meanwhile providing high-resolution and high-quality reconstruction images.

2. Theory

2.1. The Data Acquiring Process

2.1.1. CAIPIRINHA and CAIPIVAT

As mentioned in the Section. 1, the physical distance between two aliased voxels can be increased by applying the VAT, the CAIPIRINHA technique and the CAIPIVAT technique to achieve the slice-wise image shifts, thus reducing the dependence on the geometry of the coil array. The CAIPIR-INHA technique can move the FOV along the PE direction by modulating the phase for each line in k-space. Whereas the CAIPIVAT technique can shift the FOV along two directions, PE (vertical) and RO (horizontal), by applying a unique compensation gradient of VAT. Through these two image shift techniques along with the Hadamard slice encoding technique, the g-factor of the reconstructed images can be reduced. Since the g-factor is related to the signal-to-noise ratio (SNR), in SMS studies, giving the definition of the SNR (Welvaert and Rosseel (2013)):

$$SNR_{SMS} = \frac{SNR_{full}}{g\sqrt{R}}. \tag{1}$$

From Eq. 1, the SNR_{SMS} is strongly influenced by the geometric properties of the coil array, g-factor. It depends on the number and location of the coils, the phase-encoding direction, the voxel location, etc. Thus, the g-factor is not a constant number but varies across each voxel within the images (Preibisch et al. (2015)). The short physical distance between two aliased voxels will increase the g-factor value because of their intensity and sensitivity similarity which will decrease the SNR. Therefore, increasing the physical distance between two aliased voxels is one of our strategies. The VAT technique, the CAIPIRINHA technique and the CAIPIVAT technique can reduce the influence of the g-factor by applying a partial in-plane image shift. Considering the 1D inverse discrete Fourier transform, a periodic time series $y(t)$ sampled at n time points Δt apart is described as below:

$$y(p\Delta t) = \sum_{q=-\frac{n}{2}}^{\frac{n}{2}-1} f(q\Delta\nu)e^{i\frac{2\pi}{n}pq}, \tag{2}$$

where $\Delta\nu$ is the temporal frequency resolution and $\Delta\nu = \frac{1}{n\Delta t}$. It is the summation of the Fourier amplitude coefficients at multiple various frequencies.

In Eq. 2, $y(p\Delta t)$ and $f(q\Delta\nu)$ are complex-valued quantities with real and imaginary components. When we shift the whole time series from $p\Delta t$ to $p'\Delta t$, where $y(p'\Delta t)$ is same as $y(p\Delta t)$ sampled at n time points Δt apart with a different order from $y(p\Delta t)$, a field-of-view shift Δy will happen and is calculated as:

$$\Delta y = y((p - p')\Delta t) = \sum_{q=-\frac{n}{2}}^{\frac{n}{2}-1} f(q\Delta\nu)e^{i\frac{2\pi}{n}pq}e^{-i\frac{2\pi}{n}p'q}, \tag{3}$$

for $p = 1, \ldots, n$. The FOV shift only depends on the phase change in k-space, which equals $-\frac{2\pi}{n}p'q$. If $p' = 1$, which means the image moves one voxel distance in the PE direction, the modulation quantity of phase will be $-\frac{2\pi}{n}q$. If half of the image will be moved in the PE direction (FOV/2), $p' = \frac{n}{2}$, the modulation of phase should be $-\pi q$. Therefore, the phase of even lines in k-space should impart π and the phase of odd lines should impart 0. If the FOV/4 shift of the image needs to be achieved, the modulation of the phase for each line in the k-space needs to be adjusted. Figure. 2A is an illustration to explain the CAIPIRINHA process. Applying the discrete Fourier transform to each excitation in the time series to get the k-space, modulating the phase for each line in the k-space with a unique angle, after the inverse discrete Fourier transform, we will have an in-plane image shifted effect. Compared with the on-resonance spins of the CAIPIRINHA technique, during the slice-selection process, the CAIPIVAT technique allows off-resonance spins at different locations. Figure. 2B is an illustration to explain the VAT process. The VAT technique projects the excited spins along a unique view angle to map the brain with a specific spatial shift on the image plane. Figure. 2C is an illustration to explain the CAIPIVAT process. After the Fourier transform to acquire the k-space of the original image, the CAIPIRINHA technique is applied to the k-space of each slice. A global phase modulation will be added to each slice at the same time.

In this paper, the principal idea of the CAIPIRINHA technique will be applied first. For each slice within each excitation, we imply $\Delta y = (l-1)FOV/N_s$ in-plane image shift, where $l = 1, \ldots, N_s$ and N_s is the total number of aliased slices. On the TR dimension, we also imply the CAIPIRINHA technique for each excitation by $\Delta y = (m-1)FOV/N_s$ in-plane image shift, where $m = 1, \ldots, N_s$. Thus, with the in- and through-excitation image shift, at $TR = N_s+1$ excitation time point, the aliased artifacts should be the same as the $TR = 1$ excitation time point. Figure. 3A shows an example of
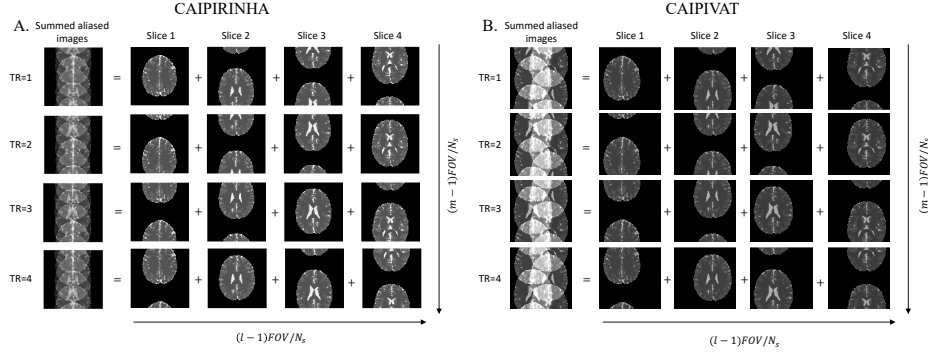
Figure 3: A. An example of in- and through-excitation image shift process with $N_s = 4$ by applying the CAIPIRINHA technique. B. An example of in- and through-excitation image shift process with $N_s = 4$ by applying the CAIPIVAT technique.

an in- and through-excitation image shift process with $N_s = 4$ incorporating with the CAIPIRINHA technique. When $TR = 5$, the image shift pattern for each slice should be the same as the time point $TR = 1$. Furthermore, the principal idea of the CAIPIVAT technique will also be applied. Similar to the CAIPIRINHA technique, $\Delta y = (l-1)FOV/N_s$ for the in-plane image shift and $\Delta y = (m-1)FOV/N_s$ for the through-plane image shift will be applied to each excitation along the PE direction. For each slice within each excitation, a unique image shift will appear horizontally on the RO direction with the support of the CAIPIVAT technique. The shift distance for each slice along the RO direction can be calculated and depends on the distance between the desired aliased slices, the compensation gradient, and the RO gradient. A modest slice-wise shift will be applied for each excitation to ensure the brain image is not outside the FOV. Figure. 3B displays an example of in- and through-excitation image shift process of $N_s = 4$ incorporating with the CAIPIVAT technique. Besides the same amount of the FOV shift in- and through-excitation on the PE direction as CAIPIRINHA technique, slice 1 and slice 3 will have a FOV shift to the left and slice 2 and slice 4 will have a FOV shift to the right on the RO direction according to the CAIPIVAT technique. Thus, comparing with the CAIPIRINHA technique approach, the overlapping area between two desired aliased images will decrease and the independence of the sensitivity for each coil will increase.

2.1.2. The Hadamard Phase Encoding

The Hadamard encoding technique is a well-developed volume excitation method. The conventional MR imaging techniques have been limited by the size of the matrix for the acquired aliased images. The Hadamard phase-encoding method allows the increment of the size of the acquired aliased image matrix by aliasing in both frequency and phase encoding dimensions. With the support of this simultaneous binary-encoded technique, the TR will decrease, and the SNR ratio will improve. The Hadamard matrix is given by:

$$H_{2^n} = \begin{bmatrix} H_{2^{n-1}} & H_{2^{n-1}} \\ H_{2^{n-1}} & -H_{2^{n-1}} \end{bmatrix} = H_2 \otimes H_{2^{n-1}}, \text{and } H_1 = \begin{bmatrix} 1 \end{bmatrix}, H_2 = \begin{bmatrix} 1 & 1 \\ 1 & -1 \end{bmatrix}, \quad (4)$$

where $\otimes$ denotes the Kronecker product. It is an orthogonal and full rank matrix with elements of either +1 or -1. In the mSPECS-CAIPIVAT study, each excitation is sequentially coordinated with a unique Hadamard aliasing pattern. To improve the computational efficiency, we select the size of the Hadamard phase-encoding matrix to be the same as the number of the aliased slices. Thus, the size of the Hadamard phase-encoding matrix is $N_s \times N_s$. In this aim, $H_{\delta,z}$ is the δth row and zth column element of Hadamard matrix corresponding to zth slice in δth TR. Same as the sequential properties of image shifts, the Hadamard phase-encoding aliasing pattern will cycle through along the TR dimension. For example, the Hadamard aliasing pattern of $TR = N_s + 1$ should be the same as $TR = 1$. Figure. 4 shows an example of the Hadamard aliasing pattern when $N_s = 4$. Figure. 4A shows a 4×4 Hadamard matrix, B shows the Hadamard coefficients for each slice in the fMRI time series, C shows the phantom brain images multiplied by Hadamard aliasing coefficients at the first 4 TRs. In order to increase the distance between two aliased voxels and reduce the influence of the g-factor, we introduce the term "packet" to indicate the slice aliasing circumstance. For example, under a circumstance with $N_s = 8$, we put odd number slices into one packet (i.e., slice 1, slice 3, slice 5, and slice 7), and even number slices into another packet (i.e., slice 2, slice 4, slice 6, and slice 8). For each excitation, all slices in one packet are measured simultaneously as one single array. Therefore, we will have 2 packets in this situation, and both packets will coordinate with the same Hadamard phase-encoding aliasing pattern. With the help of the packet technique, the slice-to-slice signal leakage artifacts will diminish.
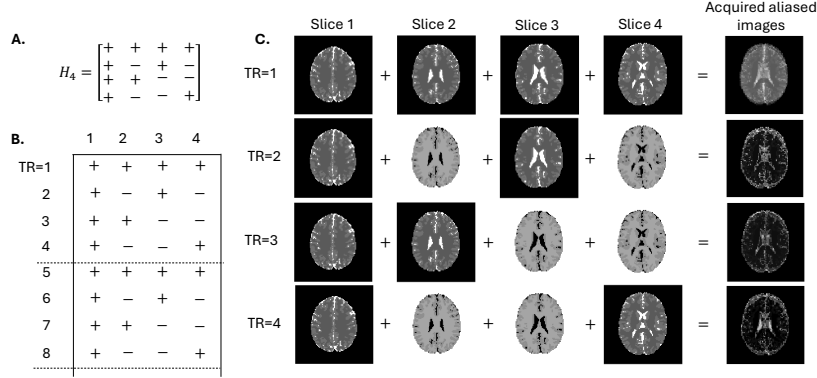
Figure 4: An illustration of Hadamard phase-encoding aliasing pattern when $N_s = 4$. A. shows the H_4 matrix with plus sign denotes as 1 and minus sign demotes as -1. B. shows sequential Hadamard aliasing coefficient for each slice in the fMRI time series. C. shows the phantom brain images are multiplied by the Hadamard aliasing coefficients at the first 4 TRs.

2.1.3. A Single Aliased Voxel

Given a single aliased voxel, $a_{j,\gamma,\delta}$, at the location (x, y) of aliased images, with δth Hadamard aliasing pattern and γth matrix rotation operation, measured at coil j, is defined as the summation equation:

$$a_{j,\gamma,\delta} = \sum_{z=1}^{N_s} H_{\delta,z} R_{\gamma,z} S_{j,z} \beta_z + \varepsilon_j. \tag{5}$$

In Eq. 5, $a_{j,\gamma,\delta}$ is a 2×1 complex-valued vector with the real and imaginary components of the acquired aliased voxel value measured at coil j, with rotating operation γ and Hadamard phase-encoding aliasing pattern δ. The Hadamard phase-encoding aliasing pattern, $H_{\delta,z}$, is the same as the definition in Section 2.1.2, where parameter δ corresponds to the order of Hadamard coefficients pattern, and parameter z corresponds to the number of slices. The coefficients of $H_{\delta,z}$ will be either +1 or -1. The matrix rotation operator, $R_{\gamma,z}$, is closely related to the definition of Section 2.1.1. Subscript γ denotes the order of the matrix rotation operation for each TR, and parameter z corresponds to the number of slices. The coil sensitivity matrix, $S_{j,z}$, is a 2×2 skew symmetric matrix with the real and imaginary components at coil j for slice z, $S_{(j, z)} = [S_R, -S_I; S_I, S_R]_{j,z}$. The true voxel value, $\beta_z = [\beta_R; \beta_I]$, is a 2×1 vector with the real and imaginary parts of the aliased voxel in slice z, and the real part is stacked on the top of the imaginary

part. The measurement noise, $\varepsilon_j = [\varepsilon_R; \varepsilon_I]$, is a 2×1 vector with real and imaginary parts stacked. The mean of measurement noise is $E(\varepsilon_j) = 0$, and the covariance of error is $cov(\varepsilon_j) = \sigma^2 I_2$, where I_2 is a 2×2 identity matrix.

Considering the measured aliased voxel in Eq. 5 across the N_c coils for N_s aliased slices with N_α time-points in the fMRI time series, Eq. 5 can be expressed as:

$$a = X_A \beta + \varepsilon. \tag{6}$$

N_α denotes the number of sequential time-points of the Hadamard encoded pattern, and it is an integer between 1 and N_s. Therefore, the net acceleration of the fMRI time series acquisition is defined as $A = N_s/N_\alpha$. In Eq. 6, the dimension of a is $2N_c N_\alpha \times 1$ including the real and imaginary components. The measurement error, ε, has the same dimension as a with the mean $E(\varepsilon) = 0$ and covariance $cov(\varepsilon) = \sigma^2 I_{2N_c N_\alpha}$. The dimension of the aliasing matrix, X_A, is $2N_c N_\alpha \times 2N_s N_r$, where N_r is an indicator of the number of matrix rotation operations. In this study, we generally assign $N_r = N_s$ to improve the computational efficiency. The true voxel value, β, has the dimension of $2N_s N_r \times 1$, including the real and imaginary value for each voxel. For the δth Hadamard aliasing pattern and γth matrix rotating operation, the aliasing matrix $(X_A)_{\gamma,\delta}$ across N_c coils is defined as:

$$(X_A)_{\gamma,\delta} = \left[H_{\delta,1} R_{\gamma,1} \begin{pmatrix} S_{1,1} \\ \vdots \\ S_{N_c,1} \end{pmatrix}, \ldots, H_{\delta,N_c} R_{\gamma,N_c} \begin{pmatrix} S_{1,N_s} \\ \vdots \\ S_{N_c,N_s} \end{pmatrix} \right]. \tag{7}$$

$R_{\gamma,z}$ is the image shift indicator which operates on coil sensitivity maps for each slice, and it is not the matrix multiplication. Across the N_α excitations, the aliasing matrix X_A can be written as:

$$X_A = \left[(X_A)_1, \ldots, (X_A)_{N_\alpha} \right]'. \tag{8}$$

Since the measurement error has a Gaussian distribution, the likelihood of the acquired aliased voxel for the N_c coils and the N_α excitations is:

$$P(a \mid X_A, \beta, \sigma^2) \propto (\sigma^2)^{-\frac{2N_c N_\alpha}{2}} \exp\left[-\frac{1}{2\sigma^2}(a - X_A\beta)'(a - X_A\beta) \right]. \tag{9}$$

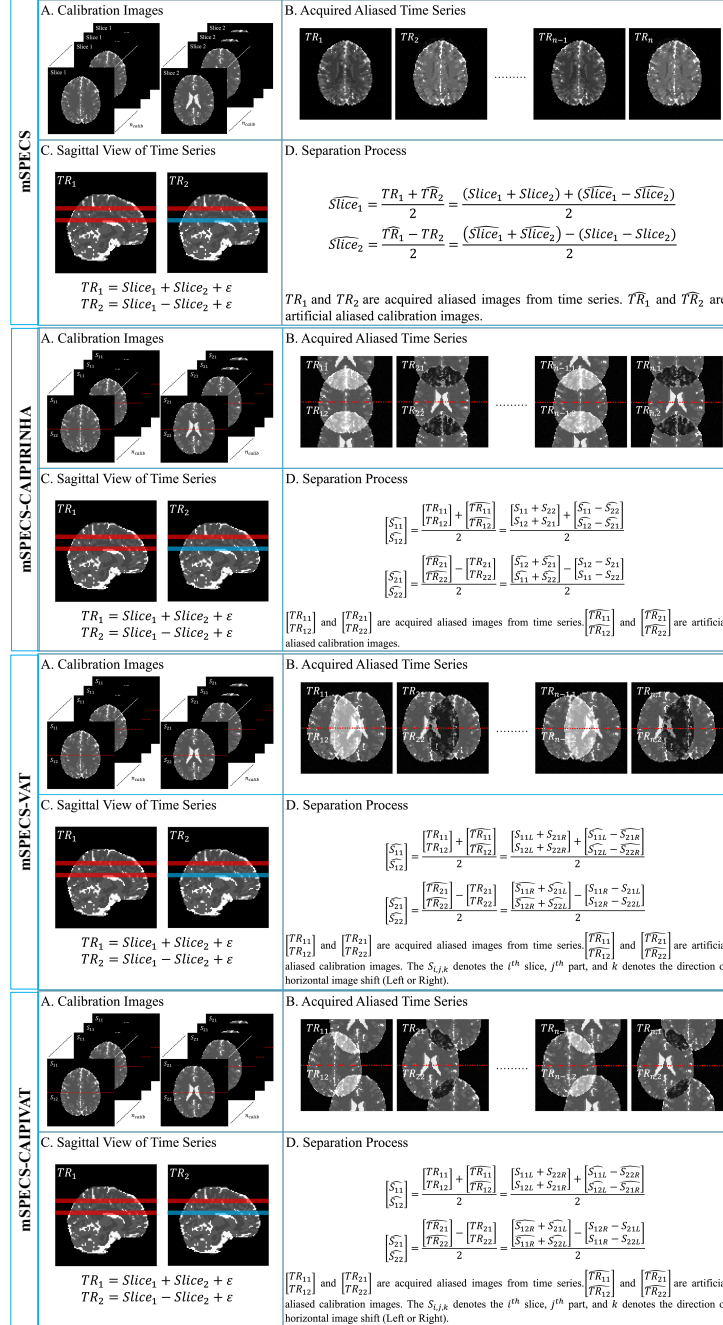To separate the aliased images and estimate the voxel value for each slice,

Figure 5: The data-acquiring process of the mSPECS technique (without any image shifts), the mSPECS-CAIPIRINHA technique (shift vertically), the mSPECS-VAT technique (shift horizontally), and the mSPECS-CAIPIVAT technique (shift vertically and horizontally).

12

the least square estimation method is used. The estimated separate voxel value, $\hat{\beta}$, can be calculated by:

$$\hat{\beta} = \left(X'_A X_A\right)^{-1} X'_A a. \tag{10}$$

Eq. 10 also can be used to calculate the reconstructed brain images in the SENSE model. In general, the determinant of X_A is close to zero, $\det(X_A) \approx 0$, which leads to failure in calculating the inverse of $X'_A X_A$. Thus, a bootstrap sampling method incorporated with artificial aliasing of reference calibration images technique are combined with the mSPECS-CAIPIVAT method. This combined technique can eliminate the inter-slice signal leakage artifacts by quantifying prior information in calibration images in a Bayesian model. More details will be shown in the following section. Figure. 5 illustrates the data-acquiring process of the mSPECS technique (without any image shifts), the mSPECS-CAIPIRINHA technique, the mSPECS-VAT technique and the mSPECS-CAIPIVAT technique.

2.2. The Bootstrap Sampling and Artificial Aliasing of Calibration Images

In the previous simultaneous multi-slice (SMS) study, bootstrap sampling and artificial aliasing of calibration reference image techniques have been proven as powerful tools to support the separation and reconstruction process of aliased images. By increasing the size of the aliasing matrix and adding a regularizer into the least square estimation function, the correlation induced by the separation process will decrease and the slice-to-slice signal leakage will be eliminated. In the fMRI time series, for each excitation, N_s bootstrap sampled coil slice images will be randomly chosen from fully sampled calibration reference images. The mean calibration image will be calculated for each slice and will be artificially aliased, which is then repeated for each TR.

Given a single TR, the calibration images will have the same shift pattern as acquired images, thus, the total number of different combinations for different voxels should be N_s, which is equal to the rank of the chosen Hadamard matrix. After removing the combination of the acquired aliasing pattern from the full voxel combination pattern, N_s-1 different combinations remain. Therefore, for a single excitation, a voxel across N_s slices, measured through N_c coils, ν, can be represented as a vector with the dimension of $2N_s N_c(N_s - 1) \times 1$ with the real component stacked on the top of the imaginary component, corresponding to the remaining combinations without the

acquired aliasing combination. The mean bootstrap sampled voxel, $\bar{\nu}$, is the same dimension as ν for each time point. The artificial aliasing calibration images, ν, across N_s slices measured through N_c coils at N_α sequential time point can be expressed as:

$$\nu = C\bar{\nu} = C_A\mu + C\eta. \tag{11}$$

The dimension of the measurement error vector, η, is the same size as the vector ν. The mean of the measurement error for the calibration images is $E(\eta) = 0$, and the covariance is $cov(C\eta) = \tau^2 I_{2N_cN_\alpha(N_s-1)}$, where $I_{2N_cN_\alpha(N_s-1)}$ is the identity matrix. It is assumed that there is no correlation between the real and imaginary components of the calibration images. The true voxel value vector, μ, is constructed with the real and imaginary components of the calibration voxel with the dimension $2N_s \times 1$. The artificial aliasing matrix, C_A, is following the same aliasing rules as acquired images do, rotating by the matrix rotation operation and multiplying the Hadamard encoding aliasing coefficients. Due to the combination of acquired aliasing voxel removed from the full combinations, the dimension of the artificial aliasing matrix is $2N_cN_\alpha(N_s - 1) \times 2N_s$. Same as the assumption in the acquired aliasing images, we assign $N_r = N_s$ to improve the computational efficiency. For example, considering a situation with $N_s = 4$ and $N_r = 4$, for each time point, $N_s - 1 = 3$ combinations should be applied for the calibration images. Thus, for a given excitation, the δth Hadamard aliasing pattern and γth matrix rotating operation, the aliasing matrix $(C_A)_{\gamma,\delta}$ across N_c coils can be written as:

$$(C_A)_{\gamma,\delta} = \left[\overline{H_{\delta,1}R_{\gamma,1}} \begin{pmatrix} S_{1,1} \\ \vdots \\ S_{N_c,1} \end{pmatrix}, \ldots, \overline{H_{\delta,N_c}R_{\gamma,N_c}} \begin{pmatrix} S_{1,N_s} \\ \vdots \\ S_{N_c,N_s} \end{pmatrix} \right]. \tag{12}$$

The notation $\overline{HR}$ denotes the remaining combination for the Hadamard encoding aliasing pattern with the matrix rotation pattern after removing the combination of the acquired aliasing pattern. Incorporating N_α sequential time points, the artificial aliasing matrix, C_A, can be written as:

$$C_A = \left[(C_A)_1, \ldots, (C_A)_{N_\alpha} \right]'. \tag{13}$$

Thus, the prior distribution of artificial aliased calibration voxel is:

$$P(\nu \mid C_A, \mu, \tau^2) \propto (\tau^2)^{-\frac{2N_cN_\alpha(N_s-1)}{2}} \exp\left[-\frac{1}{2\tau^2}(\nu - C_A\mu)'(\nu - C_A\mu) \right]. \tag{14}$$

The Eq. 6 and Eq. 11 can be combined together, which will generate:

$$y = \begin{bmatrix} a \\ \nu \end{bmatrix} = \begin{bmatrix} X_A \beta \\ C_A \mu \end{bmatrix} + \begin{bmatrix} \varepsilon \\ C\eta \end{bmatrix}. \tag{15}$$

Based on the previous section, the covariance for the acquired aliasing measurement error is $cov(\varepsilon) = \sigma^2 I_{2N_c N_\alpha}$, and the covariance for the artificial aliasing measurement error is $cov(C\eta) = \tau^2 I_{2N_s N_c (N_s-1)}$, the covariance for vector, y, consisting of acquired aliasing voxel value and the artificial aliasing voxel value is:

$$cov(y) = \begin{bmatrix} \sigma^2 I_{2N_c N_\alpha} & 0 \\ 0 & \tau^2 I_{2N_c N_\alpha (N_s-1)} \end{bmatrix}. \tag{16}$$

Without the support of the bootstrapping technique, there will be no variation in the artificial aliasing calibration images, i.e. the same calibration reference images will be artificially aliased for each TR, which will lead to $\tau^2 = 0$. However, by applying the bootstrapping technique, for each excitation, the N_s calibration images will be randomly selected and averaged to obtain $\bar{\nu}$, and hence $\tau^2 = \sigma^2$. Thus, the covariance for vector, y, is:

$$cov(y) = \sigma^2 I_{2N_c N_\alpha N_s}. \tag{17}$$

2.3. The Prior Distribution

To estimate the reconstructed voxel value separated from the aliased slices, the estimate voxel β is specified to have a normal prior distribution $\beta \sim N(\bar{\eta}, \sigma^2 (C'_A C_A)^{-1})$, therefore:

$$P(\beta \mid \sigma^2, \bar{\nu}, C_A) \propto (\sigma^2)^{-\frac{2N_s N_r}{2}} \exp\left[-\frac{1}{2\sigma^2}(\beta - \bar{\nu})'(C'_A C_A)(\beta - \bar{\nu})\right]. \tag{18}$$

The measurement error variance σ^2 specified to have a inverse gamma prior distribution:

$$P(\sigma^2 \mid \lambda, \delta) \propto (\sigma^2)^{-(\lambda+1)} \exp\left[-\frac{\delta}{\sigma^2}\right], \tag{19}$$

where hyperparameters λ and δ are assessed from the calibration images process.

2.4. The Hyperparameters Assessment — calibration images

Following the Bayesian process, the unknown hyperparameters can be assessed estimated using the prior ~~information of the Bayesian model and treated as known information~~. In the image acquisition process of the mSPECS-CAIPIVAT model, two series of brain images from two different fMRI experiments will be acquired: the calibration images and the aliased images. The aliased images correspond to the mSPECS-CAIPIVAT model, whereas the calibration images, on the other hand, are obtained using the traditional method without any image shift techniques or acceleration factors. Thus, the calibration images can be treated as prior information, and hyperparameters can be estimated from them. According to our Bayesian mSPECS-CAIPIVAT model, to estimate the voxel value β, we need to estimate the hyperparameters $\bar{\nu}$, λ, and δ. In Eq. 18, the artificial aliasing matrix C_A is a know information and it strictly follow the artificial aliasing rules in Section. 2.2. The hyperparameters $\bar{\nu}$ represents the averaged voxel value after the bootstrap resampling process, and its estimation is described in detail in Section 2.2. The hyperparameters λ and δ are shape parameter and scale parameter of the inverse-gamma distribution and we can assess them from calibration images. As discussed in the Section. 2.2, for each excitation, N_s brain images will be randomly chosen from the fully sampled calibration images and averaged to assess hyperparameter $\bar{\nu}$. Moreover, the calibration reference images can be utilized to estimate sample noise variance σ_0^2. Therefore, the hyperparameters λ and δ can be assessed by $\lambda = n_0$ and $\delta = (n_0 - 1)\sigma_0^2$. where n_0 is · · · · and σ_0^2 is · · · $\bar{\nu} = \bar{\nu}$

2.5. The Posterior Estimation

Following the Section. 2.3 and Section. 2.4, the joint posterior distribution of estimate voxel value β and the noise variance σ^2 can be obtained by combining the likelihood equation (Eq. 9), the prior distribution of β (Eq. 18) and the prior distribution of σ^2 (Eq. 19) together, that is:

$$
\begin{aligned}
P(\beta, \sigma^2 \mid \cdot) &\propto P(a \mid X_A, \beta, \sigma^2) P(\beta \mid \sigma^2, \bar{\nu}, C_A) P(\sigma^2 \mid \lambda, \delta) \\
&\propto (\sigma^2)^{-\frac{p}{2}} \exp\left[-\frac{1}{2\sigma^2}((\beta - \hat{\beta})'(X_A'X_A + C_A'C_A)(\beta - \hat{\beta}) + w) \right],
\end{aligned} \tag{20}
$$

where $p = 2N_cN_\alpha + 2N_sN_r - 2\lambda - 2$, and $w = a'a + \bar{\nu}'C_A'C_A\bar{\nu} - (X_A'a + C_A'C_A\bar{\nu})'(X_A'X_A + C_A'C_A)^{-1}(X_A'a + C_A'C_A\bar{\nu}) + 2\delta$. After integration, the

16

marginal posterior distribution of estimate voxel value β is a student-t distribution and the marginal posterior distribution of σ^2 is a inverse gamma distribution. Thus, the least squares estimation function is incorporated with the mSPECS-CAIPIVAT method, which will lead us to:

$$\hat{\beta} = (X_A'X_A + C_A'C_A)^{-1}(X_A'a + C_A'\overline{\nu}). \tag{21}$$

$C_A'C_A$ works as the regularizer for matrix inverse to improve the condition of the equation. The posterior mean of the estimated voxel is:

$$E(\hat{\beta}) = (X_A'X_A + C_A'C_A)^{-1}(X_A'X_A\beta + C_A'C_A\mu). \tag{22}$$

IS $\mu \approx \beta$ so that $E(\hat{\beta}) = \beta$?

Moreover, the covariance of $\hat{\beta}$ is:

$$cov(\hat{\beta}) = \sigma^2(X_A'X_A + C_A'C_A)^{-1}; \tag{23}$$

the separated (estimated) voxel values are uncorrelated.

3. Simulation Study

and $\hat{\sigma}^2 = ?$ var($\hat{\sigma}^2$) = ? What about making images of these?

3.1. Simulated FMRI Data

To investigate the performance of our proposed novel SMS technique, the mSPECS-VAT, the mSPECS-CAIPIRINHA and the mSPECS-CAIPIVAT model were applied to simulated fMRI data, and the results were compared with the mSPECS and the standard SENSE method. The simulated fMRI data has $TR = 510$ time points and mimics the real-world right hand finger tapping fMRI experiment. The first 20 time points will be omitted, thus leaving the simulated fMRI data with 490 time points. To replicate the full process of the real right-handed finger-tapping experiment, two time series were generated from the true noiseless axial view data: the calibration simulated data, and the task simulated data. The calibration simulated data includes $N_S = 8$ axial brain images without any simulated task activation blocks for each image. The task simulated data, in contrast, includes $N_S = 8$ axial brain images with simulated task activation blocks on the left motor cortex for the first 4 slices. No simulated activation blocks were added to the other 4 slices. The simulated activation blocks were added according to the in vivo experiment design, with the first 20 TRs off, following 15 TRs on and 15 TRs off for 16 epochs, and the last 10 TRs off. To achieve the $CNR = 0.5$, the mean magnitude of 0.04 was added to the simulated activation blocks for the first 4 slices. The mean magnitude of 4, to achieve $SNR = 50$, and different phase angles from 5° to 40° with 5° intervals were added to each
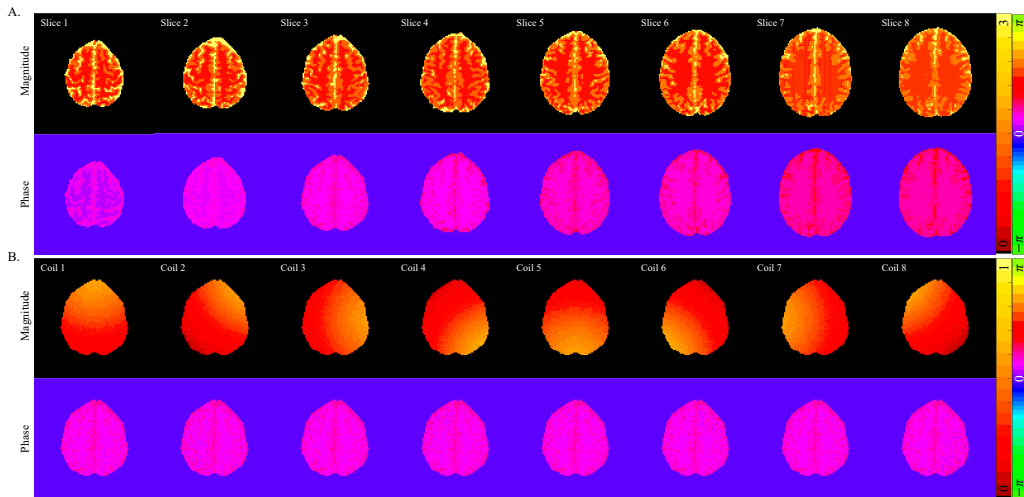
17

Figure 6: A. The true noiseless simulated magnitude and true phase information for axial brain images. B. The simulated magnitude and phase information of $N_C = 8$ channels coil for slice 3.

image. In order to further increase the distinction of the spatial information for different tissue type, angle 7.5° was added to white matter (WM), 15° was added to gray matter (GM), and 22.5° was added to the cerebral spinal fluid (CSF). Gaussian distribution noise $N(0, 0.0064)$ was added for each image of the calibration simulated data and the task simulated data separately. Figure. 6A shows the true noiseless simulated magnitude and true phase information for $N_S = 8$ axial brain images.

A total of $N_C = 8$ channel coil sensitivity profiles were simulated to weight each axial brain image. A mean magnitude of 0.95 and the different phase angles from 0° to 17.5° with 2.5° intervals were applied to each coil sensitivity. Figure. 6B shows the simulated magnitude and phase information of the $N_C = 8$ channel coil sensitivity profiles for the third axial brain image (slice 3). In the interest of investigating our new proposed SMS techniques under different TPA factors, we applied our model to three acceleration scenarios: TPA=2 (packet 1: slice 1 and 5, packet 2: slice 2 and 6, packet 3: slice 3 and 7, and packet 4: slice 4 and 8), TPA=4 (packet 1: slice 1, 3, 5 and 7, packet 2: slice 2, 4, 6 and 8), and TPA=8 (all slices into one packet). The number of packets multiplied by the acceleration factor equals to the total number of images. All experiments were performed on MATLAB program software.
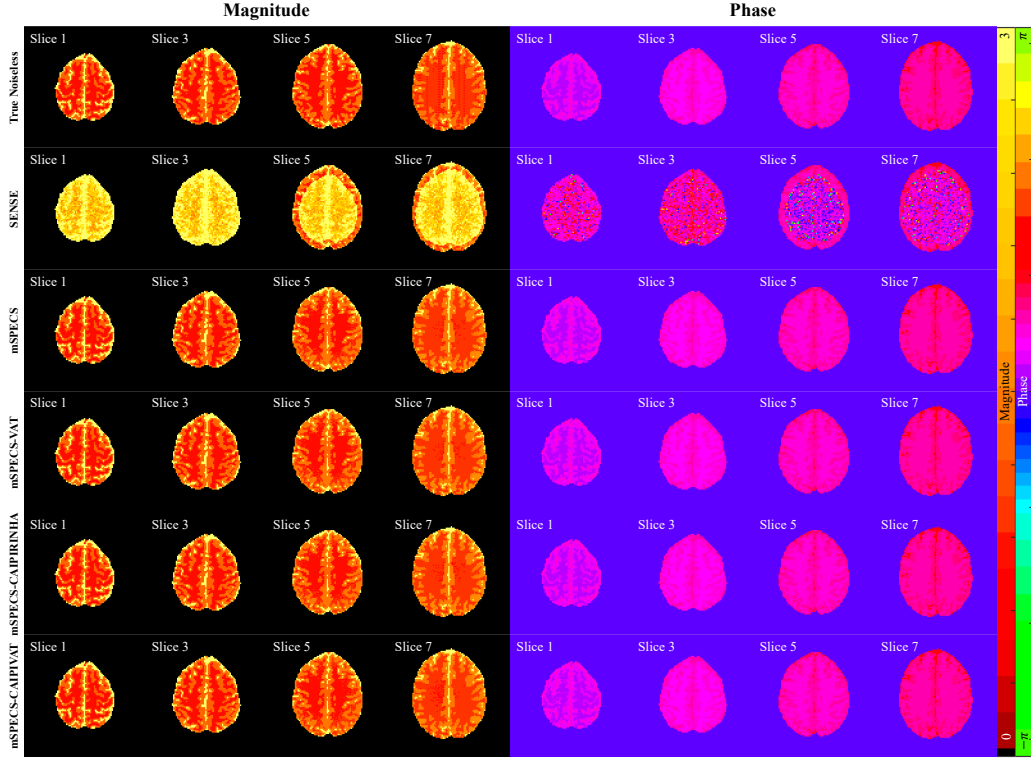
Figure 7: The true noiseless simulated magnitude and phase of the axial brain images compared with the temporal mean magnitude and temporal mean phase from SENSE, mSPECS, mSPECS-VAT, mSPECS-CAIPIRINHA and mSPECS-CAIPIVAT model for odd slices with TPA=2.

3.2. Non-Task Simulated Reconstruction Results

Following the methodology of the novel slice-wise image shift SMS technique, we conducted the simulated experiment using different through-plane acceleration factors: TPA=2, TPA=4, and TPA=8. We compared the reconstruction results under the same acceleration factors from the mSPECS model and the standard SENSE model. Figure. A.14 shows the temporal mean magnitude and phase of the reconstructed images from SENSE, mSPECS, mSPECS-VAT, mSPECS-CAIPIRINHA and mSPECS-CAIPIVAT model compared with the true magnitude and the phase of the brain images for odd slices with acceleration factor TPA=2. The simulated reconstruction results for even slices of the four models can be found in Appendix A. As shown in Figure. A.14, the mean magnitude and phase of the recon-
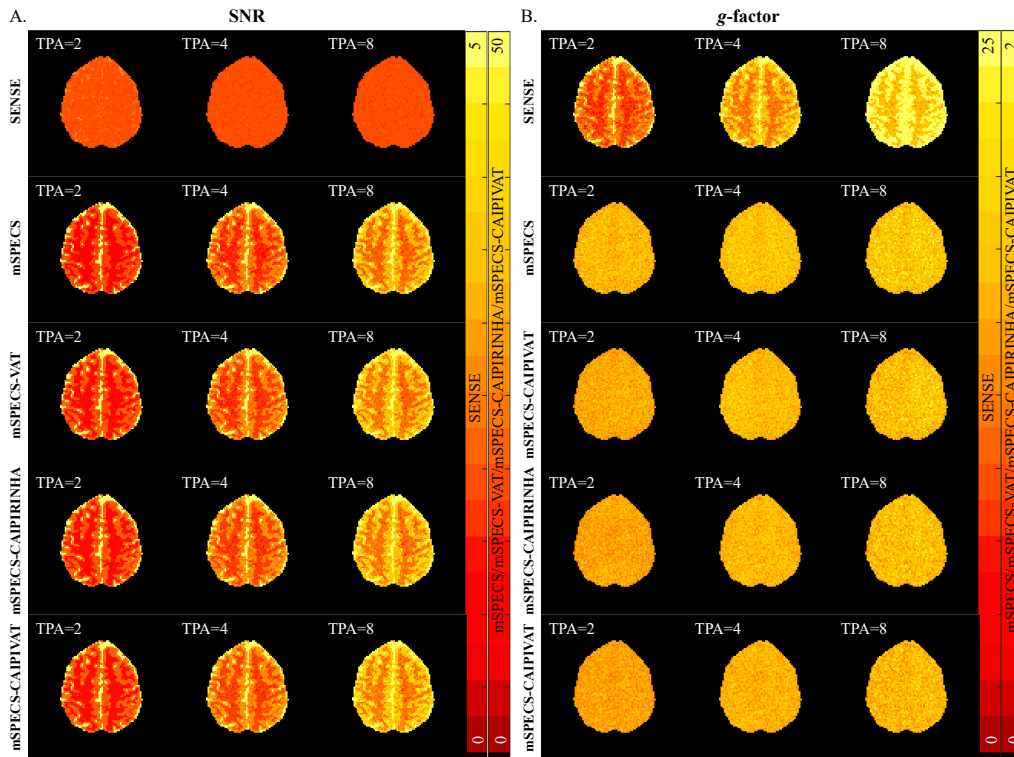
19

Figure 8: A. The *SNR* maps for SENSE, mSPECS, mSPECS-VAT, mSPECS-CAIPIRINHA and mSPECS-CAIPIVAT model with TPA=2, TPA=4, and TPA=8. The higher *SNR*, the better model performs. B. The *g*-factor maps for SENSE, mSPECS, mSPECS-VAT, mSPECS-CAIPIRINHA and mSPECS-CAIPIVAT model with TPA=2, TPA=4, and TPA=8. The closer *g*-factor is to 1, the better model performs.

structed images from the mSPECS, mSPECS-VAT, mSPECS-CAIPIRINHA, and mSPECS-CAIPIVAT models closely match the true values, indicating that these three models produce more accurate reconstructions. In contrast, the SENSE model yields the poorest reconstructions, with noticeable signal leakage from other aliased slices. As the acceleration factor increases to TPA=4 and TPA=8, the mSPECS, mSPECS-VAT, mSPECS-CAIPIRINHA, and mSPECS-CAIPIVAT models continue to provide reconstructions that closely resemble the true images. However, the reconstruction quality from the SENSE model significantly deteriorates, showing the worst performance among the four models.

The *SNR* value and *g*-factor value were also compared across four models.

The temporal signal-to-noise ratio is defined as $SNR = \bar{S}/\sigma_N$, where $\bar{S}$ is the mean magnitude value in the time series, and σ_N is the standard deviation of the noise. The signal-to-noise ratio also can be expressed as $SNR = \beta_0/\sigma_N$, where β_0 is the baseline signal, and σ_N is the standard deviation of the magnitude of the noise. Based on the definition of SNR in Section 2.1.1, the g-factor can be calculated as $g_{accelerate} = \sqrt{N_s}SNR_{full}/SNR_{accelerate}\sqrt{R}$, where SNR_{full} is the SNR map from model without acceleration technique, and R indicates the in-plane acceleration factor, which in this case $R = 1$ (Welvaert and Rosseel (2013)). The g-factor also indicates the noise amplification level of the model. Figure. 8 shows the temporal SNR map and g-factor map for the standard SENSE, mSPECS, mSPECS-VAT, mSPECS-CAIPIRINHA and mSPECS-CAIPIVAT models with through-plane acceleration factors TPA=2, TPA=4, and TPA=8 for slice 3. From Figure. 8, we observe that the standard SENSE model produces a low SNR map and a high g-factor penalty for all acceleration factors compared to the other four models. Increasing the through-plane acceleration factors reduces the SNR value and significantly increases the g-factor penalty. Although the mSPECS model offers a relatively good SNR map, the g-factor penalty increases as the through-plane acceleration factors rise. The mSPECS-VAT, mSPECS-CAIPIRINHA and mSPECS-CAIPIVAT models, however, provide better SNR and g-factor maps, with higher SNR values and lower g-factor penalties. As the through-plane acceleration factor increases, the SNR maps become brighter, indicating an increase in SNR, while the g-factor penalties remain relatively steady, as shown in Figure. 8.

3.3. Task Simulated Reconstruction Results

We also applied the novel slice-wise image shift SMS models to the simulated right-handed finger-tapping fMRI data with different through-plane acceleration factors TPA=2, TPA=4, and TPA=8, and compared the task activation results between each method. In the interest of further exploring the task detection ability for each model, two important criteria, the contrast-to-noise (CNR) value and the activation detection maps were also investigated. The CNR ratio is calculated as $CNR = \beta_1/\sigma_N$, where β_1 represents the task activation signal contrast. Activation detection was performed using a complex-valued model to compute fMRI activation (Rowe and Logan (2004)). Figure. A.16A shows the CNR map for SENSE, mSPECS, mSPECS-VAT, mSPECS-CAIPIRINHA and mSPECS-CAIPIVAT model for odd slices at TPA=2, and the average CNR value and standard deviation of CNR value
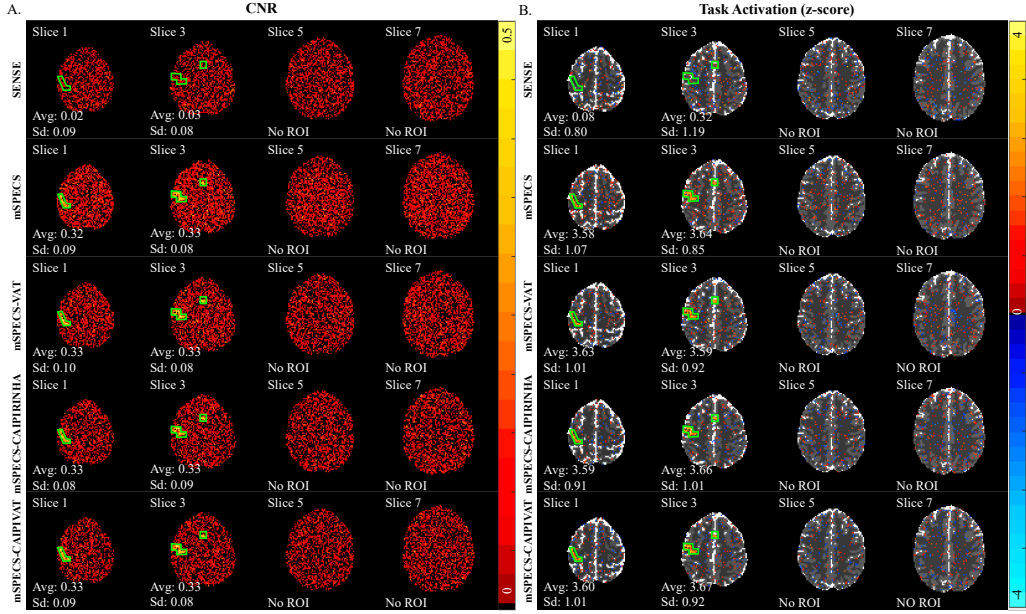
21

Figure 9: A. The *CNR* map and the average *CNR* value and standard deviation of *CNR* of ROI for SENSE, mSPECS, mSPECS-VAT, mSPECS-CAIPIRINHA and mSPECS-CAIPIVAT model for odd slices with TPA=2. B. The activation detection map and the average and standard deviation of z-score of ROI for SENSE, mSPECS, mSPECS-VAT, mSPECS-CAIPIRINHA and mSPECS-CAIPIVAT model for odd slices with TPA=2.

for region-of-interest (ROI). The *CNR* and the average *CNR* value and standard deviation of *CNR* value for region-of-interest (ROI) for four model of even slices can be found in Supplement Material Section S-2 (**?**). Since no simulated activation blocks were added to the last four slices, *CNR* values were not captured from those regions. In Figure. A.16A, the SENSE model fails to capture any activation signal within the brain, while the mSPECS, mSPECS-VAT, mSPECS-CAIPIRINHA, and mSPECS-CAIPIVAT models successfully capture the simulated activation blocks with clear shapes and anatomical details. When comparing the average *CNR* value of the ROI, the mSEPCS-VAT, mSPECS-CAIPIRINHA and mSPECS-CAIPIVAT models demonstrate slightly higher values than the mSPECS model with TPA=2. To further examine the influence of the acceleration factor on activation detection, we compared the *CNR* maps of the four models at different acceleration factors. Figure. 10A displays the *CNR* maps from the SENSE, mSPECS, mSPECS-VAT, mSPECS-CAIPIRINHA, and mSPECS-CAIPIVAT models
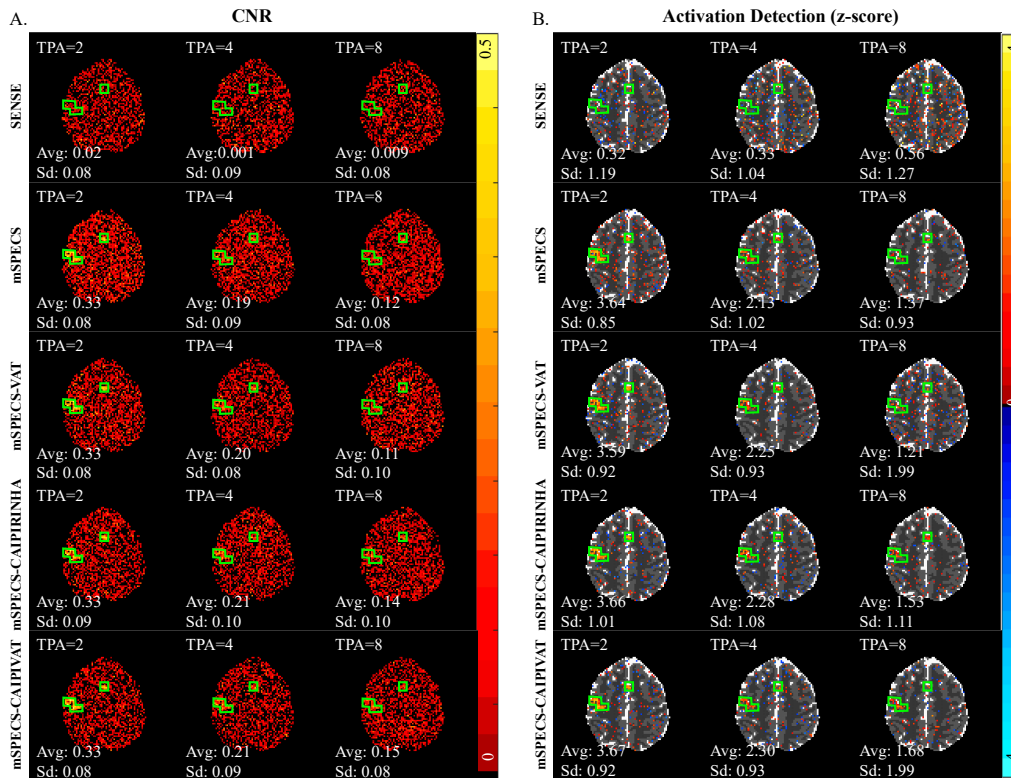
22

Figure 10: A. The *CNR* maps and average ROI *CNR* value from SENSE, mSPECS, mSPECS-VAT, mSPECS-CAIPIRINHA and mSPECS-CAIPIVAT model with respect to different acceleration factors TPA=2, TPA=4, and TPA=8 for slice 3. B. The task activation detection maps and average ROI z-score from SENSE, mSPECS, mSPECS-CAIPIRINHA and mSPECS-CAIPIVAT model with repect to acceleration factor TPA=2, TPA=4 and TPA=8 for slice 3. The higher *CNR* and z-score, the better model performs.

for TPA=2, TPA=4, and TPA=8 in slice 3. As the acceleration factor increases, the average *CNR* value of the ROI decreases for the mSPECS, mSPECS-VAT, mSPECS-CAIPIRINHA, and mSPECS-CAIPIVAT models. However, the average *CNR* value in the three slice-wise image-shifting models remains slightly higher than in the mSPECS model. In contrast, the SENSE model fails to capture any simulated activation blocks at any acceleration factor. The mSPECS-CAIPIVAT provides the highest average *CNR* of ROI among the three slice-wise image-shifting models with higher acceleration factors.

Concerning the main goal of this study is to improve the task activa-

tion detection rate, we also examined the activation detection map across four models. Figure. A.16B shows the activation detection maps for odd slices from SENSE, mSPECS, mSPECS-VAT, mSPECS-CAIPIRINHA and mSPECS-CAIPIVAT model for odd slices at acceleration factor TPA=2. The activation detection maps for even slices from four models can be found in Appendix A. Similar to the results observed in the *CNR* map, it is difficult to capture the simulated task activation blocks by applying the SENSE model. Additionally, the average z-score of ROI from SENSE model is the lowest among five models. In contrast, the mSPECS, mSPECS-VAT, mSPECS-CAIPIRINHA, and mSPECS-CAIPIVAT models can capture the simulated task activation blocks with complete shapes and anatomical structures. Comparing the average z-scores of the ROI from these three models, the three slice-wise image-shifting models, mSPECS-VAT, mSPECS-CAIPIRINHA and mSPECS-CAIPIVAT, exhibit higher significance levels than the mSPECS model. The mSPECS-CAIPIVAT model provides the highest average z-score of the ROI, indicating that it is more powerful in detecting activation signals than the other models. Similarly, we applied the four models with different acceleration factors to further investigate the activation detection process. Figure. 10B shows the task activation detection maps from the SENSE, mSPECS, mSPECS-VAT, mSPECS-CAIPIRINHA, and mSPECS-CAIPIVAT models at acceleration factors of TPA=2, TPA=4, and TPA=8 for slice 3. As the acceleration factor increases, the SENSE model fails to capture any task activation signals, and the average z-score of the ROI remains the lowest among the four models. The average z-score of the ROI from the mSPECS, mSPECS-VAT, mSPECS-CAIPIRINHA, and mSPECS-CAIPIVAT models decreases with increasing acceleration factor, and it becomes more challenging to capture the full shape of the task activation blocks. However, consistent with the *CNR* map results, the three slice-wise image-shifting models provide higher average z-scores of the ROI compared to the mSPECS model. The mSPECS-CAIPIVAT model offers the highest average z-score, confirming that it is more effective in detecting activation signals than the other models.

4. Experimental FMRI Study

4.1. Experimental FMRI Data

A 3.0 T General Electric Signa LX MRI scanner was used to perform a right-handed finger-tapping fMRI experiment on a single object. The ex-

periment was designed with an initial 20s of rest, following 15s off and 15s on for 16 epochs, and a final 10s of rest. This results in a time series with 510 time repetitions was acquired for each repetition lasting 1s. The first 20s were disregarded leading to a time series with 490 time repetitions. An additional non-task time series was also acquired from the same object to serve as calibration time series. A flip angle of 90° with an acquisition bandwidth of 125kHz was applied in this experiment. The thickness of the axial brain images slice was 2.5 mm with 9 slices for each time repetition. Due to the nature of the Hadamard phase-encoding method, 8 slices were used to the new proposed reconstruction models and compared with the existing models. The most interior axial brain slice was disregarded. An 8 channel receiver coil was applied with dimension 96×96 for a 24 cm full FOV. The phase encoding direction is posterior to anterior. In order to acquire the 'true' reconstruction brain images and activation signals, the SENSE model was applied to each time repetition without any through-plane acceleration method, and the reconstructed images were treated as reference reconstruction images. Reconstruction results from SENSE, mSPECS, mSPECS-VAT, mSPECS-CAIPIRINHA and mSPECS-CAIPIVAT model were compared to the reference reconstruction images.

4.2. Non-Task Experimental Reconstruction Results

In order to investigate the performance of the new slice-wise image shift SMS models on a real-world experiment, we applied mSPECS-VAT, mSPECS-CAIPIRINHA and mSPECS-CAIPIVAT model to the right-handed finger-tapping fMRI experiment time series. Reconstructed axial brain images were obtained from these three image shifting models and compared with the reconstruction results from SENSE and mSPECS models; reference images were also included in the comparison. We also investigated the model performance of the new slice-wise image shift models with different acceleration factors TPA=2, TPA=4 and TPA=8, and compared the reconstruction results with the SENSE and mSPECS model. Figure. A.17 shows the temporal mean magnitude and mean phase of the reconstructed images from the reference, SENSE, mSPECS, mSPECS-VAT, mSPECS-CAIPIRINHA, and mSPECS-CAIPIVAT model for odd slices with acceleration factor TPA=2. The temporal mean magnitude and mean phase for even slices of four models can be found in Appendix A. From Figure. A.17, compared with the reference axial brain images, the reconstructed images from the SENSE model exhibit strong signal leakage from aliased slices, making anatomical structures
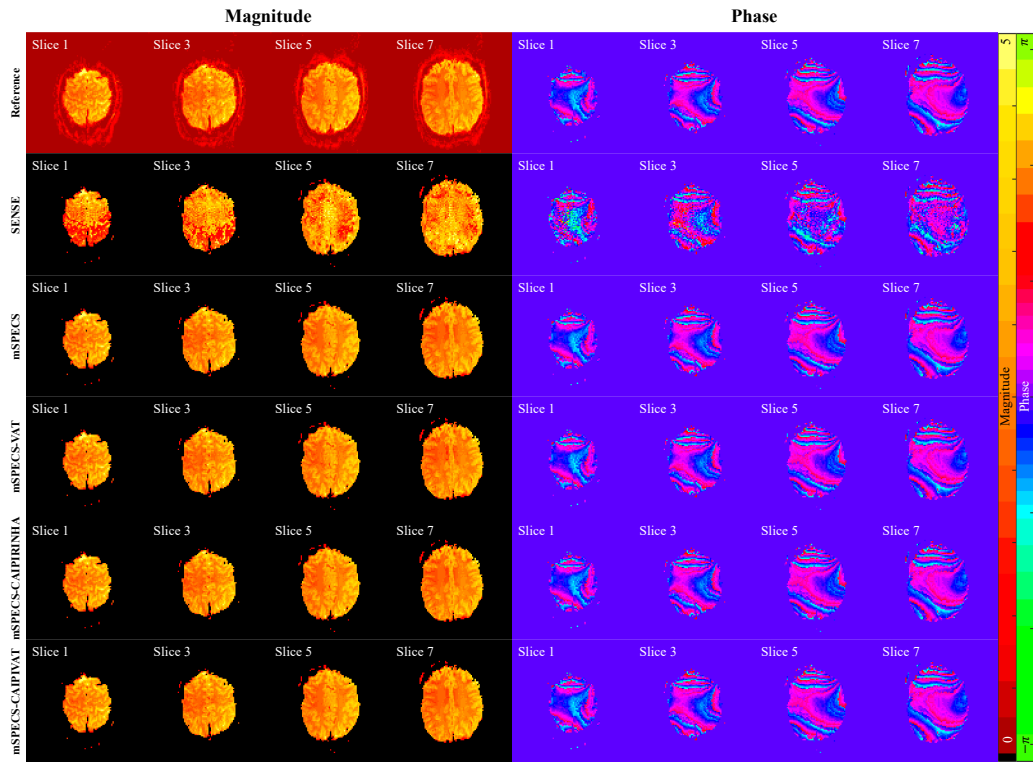
25

Figure 11: The temporal mean magnitude and temporal mean phase of the axial brain images from the reference, SENSE, mSPECS, mSPECS-VAT, mSPECS-CAIPIRINHA, and mSPECS-CAIPIVAT for odd slices with acceleration factor TPA=2.

difficult to discern. In contrast, the reconstructed images from the mSPECS, mSPECS-VAT, mSPECS-CAIPIRINHA, and mSPECS-CAIPIVAT models closely resemble the reference images, with clear anatomical structures visible.

Similar to the simulation reconstruction results section, we also investigated the SNR value and g-factor value of the reconstructed axial brain images of the four models. Figure. 12 shows the average and standard deviation of SNR value and g-factor value of ROI of reconstructed images for SENSE, mSPECS, mSPECS-VAT, mSPECS-CAIPIRINHA and mSPECS-CAIPIVAT model with different acceleration factors. From Figure. 12A, as the acceleration factor increases, the average SNR value of the ROI from the SENSE model decreases, whereas the average SNR values from the other three models increase. Comparing the mSPECS and the two slice-wise image
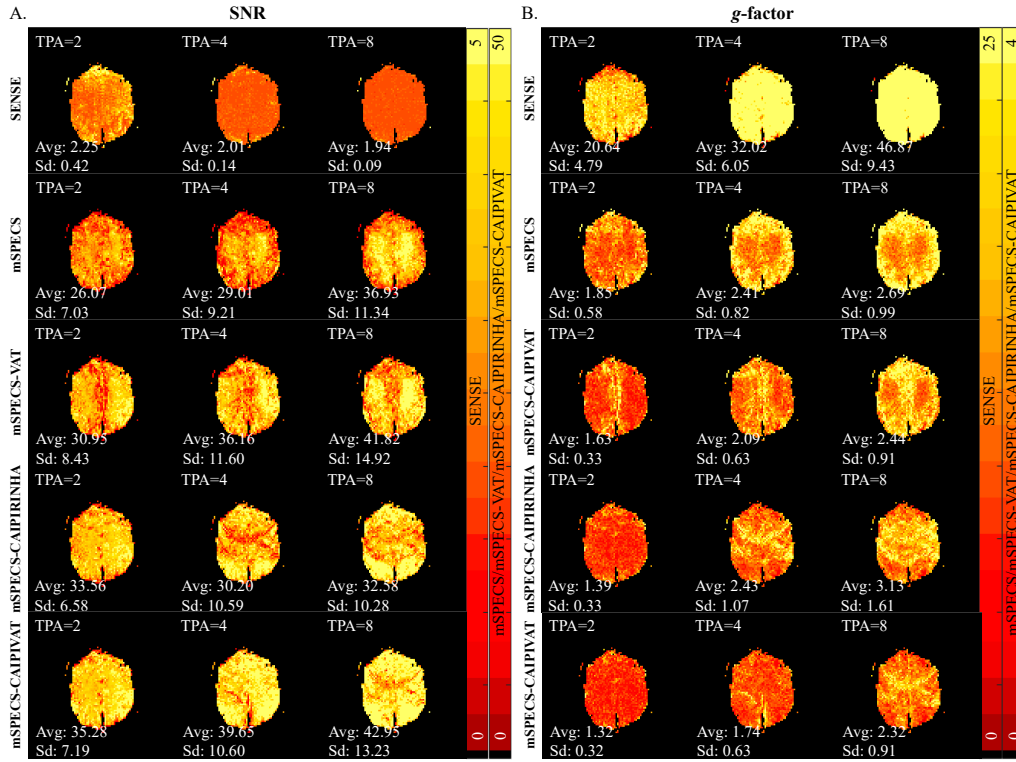
Figure 12: A. The *SNR* maps for SENSE, mSPECS, mSPECS-VAT, mSPECS-CAIPIRINHA and mSPECS-CAIPIVAT model with TPA=2, TPA=4, and TPA=8. B. The *g*-factor maps for SENSE, mSPECS, mSPECS-VAT, mSPECS-CAIPIRINHA and mSPECS-CAIPIVAT model with TPA=2, TPA=4, and TPA=8.

shift techniques, the mSPECS-CAIPIVAT model provides the highest average *SNR* value of the ROI among these three models. From Figure. 12B, as the acceleration factor increases, the average *g*-factor value of the ROI from the SENSE model increases dramatically. On the other hand, similar to the results from the simulation reconstruction study, the average *g*-factor values of the ROI from the mSPECS, mSPECS-VAT, mSPECS-CAIPIRINHA, and mSPECS-CAIPIVAT models increase slightly, with the mSPECS-CAIPIVAT model providing the lowest average *g*-factor value among these four models.
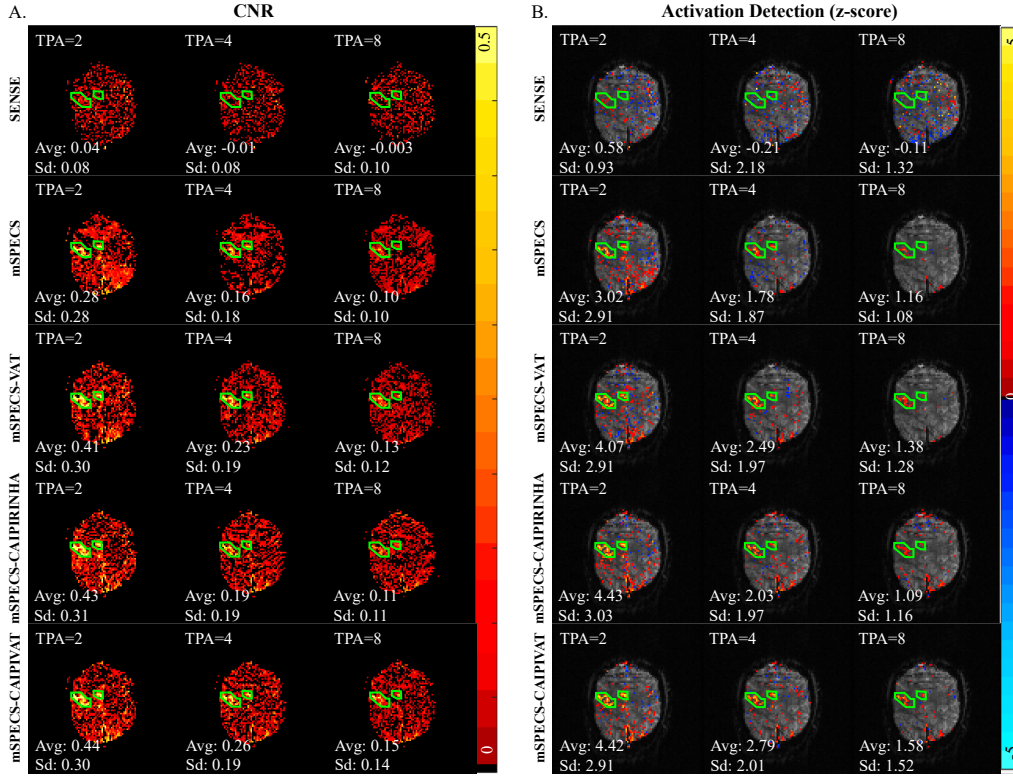
Figure 13: A. The *CNR* maps and average ROI *CNR* value from SENSE, mSPECS, mSPECS-VAT, mSPECS-CAIPIRINHA and mSPECS-CAIPIVAT model with respect to different acceleration factors TPA=2, TPA=4, and TPA=8 for slice 3. B. The task activation detection maps and the average ROI z-score from SENSE, mSPECS, mSPECS-VAT, mSPECS-CAIPIRINHA and mSPECS-CAIPIVAT model with respect to acceleration factor TPA=2, TPA=4 and TPA=8 for slice 3. The higher *CNR* and z-score, the better model performs.

4.3. Task Experimental Reconstruction Results

We also investigated the activation signal detection of the new proposed slice-wise image shift model by analyzing the *CNR* value map and the activation detection maps and comparing the reconstructed results with the SENSE and mSPECS model. We compared the average *CNR* value of ROI between different models with different acceleration factors. Figure. 13A shows the *CNR* map for SENSE, mSPECS, mSPECS-VAT, mSPECS-CAIPIRINHA and mSPECS-CAIPIVAT model with TPA=2, TPA=4 and TPA=8. As the acceleration factor increases, the SENSE model cannot capture any acti-

vation signals. Furthermore, the average *CNR* value of the ROI decreases for the mSPECS, mSPECS-VAT, mSPECS-CAIPIRINHA, and mSPECS-CAIPIVAT models as the acceleration factor increases, indicating that as the number of aliasing slices increases, the activation blocks become harder to detect. However, the two slice-wise image-shifting techniques still provide higher average *CNR* values for the ROI than the mSPECS model, with the mSPECS-CAIPIVAT model providing the highest score. This means that the mSPECS-CAIPIVAT model is more powerful than the other three models in detecting activation blocks.

The activation detection maps were also investigated. Figure. 13B shows the activation detection map and the average z-score of ROI from four models with different acceleration factors TPA=2, TPA=4 and TPA=8. The SENSE model cannot detect any activation blocks with any acceleration factor. Additionally, as the acceleration factor increases, the average z-score of the ROI decreases for the mSPECS, mSPECS-VAT, mSPECS-CAIPIRINHA, and mSPECS-CAIPIVAT models, indicating that detecting activation blocks becomes more challenging with more aliasing slices. However, when comparing the mSPECS model with the image-shifting techniques, the slice-wise image-shifting models provide higher average z-scores of the ROI, with the mSPECS-CAIPIVAT model having the highest average z-score. Thus, we reach the same conclusion as in the simulation study: the mSPECS-CAIPIVAT model is more powerful in detecting activation signals compared to the other models.

5. Discussion

Since fMRI studies were first introduced by Ogawa et al. (1990), efforts have been made to enhance the efficiency of the signal acquisition procedure but still be able to achieve the goal of reconstructing brain images with high resolution, and improve the accuracy to capture the brain activation signal. Parallel imaging reconstruction methods, like SENSE, can be a potential solution to shorten the scan time with a through-plane subsampling technique. However, it is easily influenced by the high similarity of weighted coil sensitivity information of two aliased voxels, which leads to the singular matrix problem and the inter-slice signal leakage problem in the reconstruction process. In the interest of decreasing the similarity and increasing the independence of the weighted information of aliased voxels, slice-wise imaging shift techniques, CAIPIRINHA and CAIPIVAT, can increase the

physical distance of the aliased voxels. Compared to techniques without the image-shifting method, like the SENSE and mSPECS, the mSPECS-VAT, the mSPECS-CAIPIRINHA and the mSPECS-CAIPIVAT methods can provide reconstructed brain images with more anatomic details and the reduced temporal variance.

We also compared the average SNR values for different tissue types and the average g-factor values of these four models with respect to the different through-plane acceleration factors (Appendix A). Moreover, comparing the g-factor penalty among four models with respect to different acceleration factors, the mSPECS-CAIPIVAT model has the lowest value, which means that the mSPECS-CAIPIVAT model has a lower noise amplification level compared with other models. Thus, the image reconstruction method with slice-wise image shift techniques, mSPECS-VAT, mSPECS-CAIPIRINHA and mSPECS-CAIPIVAT, produce better results by increasing the SNR values and decreasing the variance of the reconstructed images. However, as shown in Figure. 10, increasing the through-plane acceleration factor leads to a loss in the average CNR values and the mean activation values of the task block when comparing the mSPECS, mSPECS-VAT, mSPECS-CAIPIRINHA, and mSPECS-CAIPIVAT models. With TPA increasing from 2 to 8, the mSPECS model shows a 63% decrease in CNR and a 62% decrease in mean activation. For the mSPECS-VAT model, CNR decreases by 66% and mean activation by 66%, the mSPECS-CAIPIRINHA model, CNR decreases by 63% and mean activation by 58%, while the mSPECS-CAIPIVAT model shows decreases of 54% for both CNR and mean activation. Thus, comparing these four models, the SENSE model yields the worst results with strong inter-slice signal leakage. Compared to the mSPECS model, the slice-wise image shift SMS models have higher SNR and CNR values with lower g-factor penalty under circumstance with high acceleration factors. Similar conclusion can be made from Figure. 13, comparing with the mSPECS model, the slice-wise image shift techniques provide us higher SNR value for ROI and lower g-factor penalty under the circumstance with high acceleration factor like TPA=8. However, we still need to face the situation where, with the high acceleration factor, the loss of the CNR value and the activation detection rate becomes significant. Therefore, by comparing the average CNR values for ROI and activation detection maps among the four models, the mSPECS-CAIPIVAT model provides us the best CNR and activation detection map.

In this study, we discussed SMS models employing different slice-wise im-

age shift techniques. Intuitively, the smaller the overlapping area between aliased slices, the easier it is to separate them. Therefore, we compared the completely overlapping case, mSPECS model, with slice-wise image shift techniques, including mSPECS-VAT (horizontal), mSPECS-CAIPIRINHA (vertical), and mSPECS-CAIPIVAT (horizontal and vertical). Compared to slice-wise image shift techniques that operate in only one direction, as in mSPECS-VAT and mSPECS-CAIPIRINHA, the mSPECS-CAIPIVAT model utilizes shifts in both directions, resulting in a smaller overlapping area and consequently better reconstruction results. By roughly comparing the results from the simulation reconstruction section and the experimental reconstruction section of the mSPECS-VAT, the mSPECS-CAIPIRINHA model and the mSPECS-CAIPIVAT model and to make a fair decision through a trade-off of the increment in the SNR and decrement of the CNR value and the activation detection with respect to different acceleration factors, we suggest the optimal through-plane acceleration factor to be TPA=4. Under this circumstance, the mSPECS-CAIPIVAT model can provide reconstructed images with high SNR information, but still be able to capture the activation signal. Our suggestion is consistent with the optimal multiband factor MB=4 from previous work (Risk et al. (2021)).

6. Acknowledgments

Appendix A. Supplement to Simulation Study and Experimental FMRI Study

Appendix A.1. Non-Task Simulated Reconstruction Results

In Subsection. 3.2 of the main paper, we presented the temporal mean magnitude and temporal mean phase of the reconstructed axial brain images from odd slices using the SENSE, mSPECS, mSPECS-VAT, mSPECS-CAIPIRINHA, and mSPECS-CAIPIVAT models, and compared them with the true noiseless magnitude and phase. Figure. A.14 displays the temporal mean magnitude and temporal mean phase for the even slices of the reconstructed axial brain images with TPA=2. Significant signal leakage can be
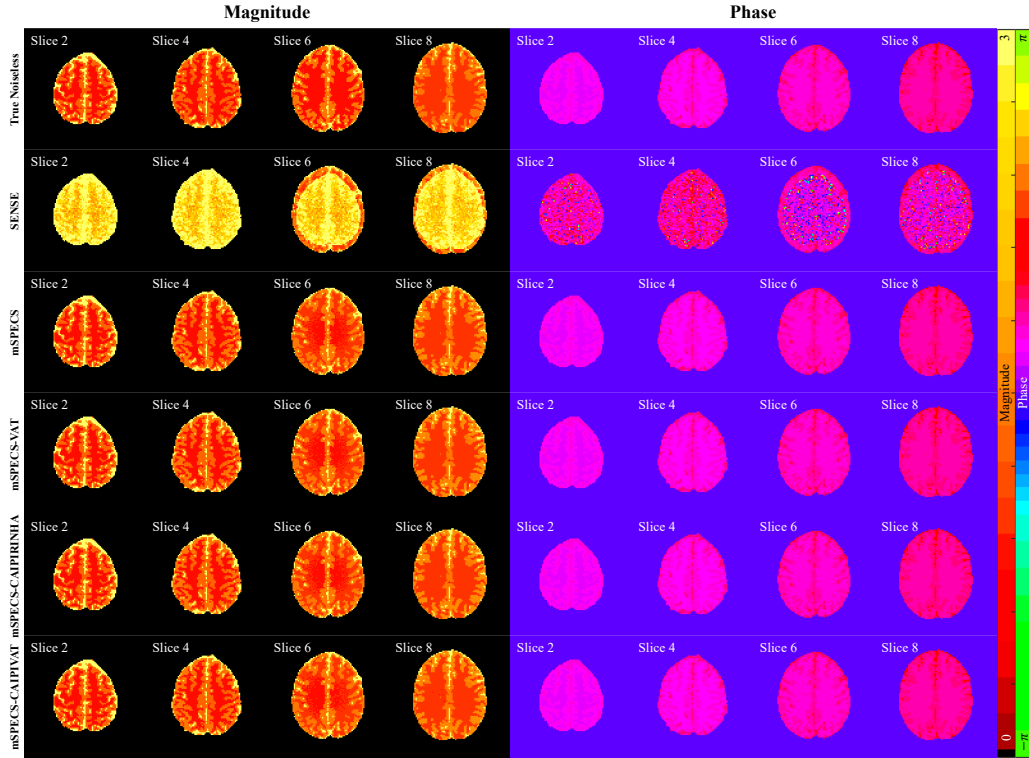
Figure A.14: The true noiseless simulated magnitude and phase of the axial brain images compared with the temporal mean magnitude and temporal mean phase from SENSE, mSPECS, mSPECS-VAT, mSPECS-CAIPIRINHA and mSPECS-CAIPIVAT model for even slices with TPA=2.

observed in the reconstructed images from the SENSE model, whereas the temporal mean magnitude and temporal mean phase from the mSPECS, mSPECS-VAT, mSPECS-CAIPIRINHA, and mSPECS-CAIPIVAT models closely match the true noiseless magnitude and phase. To further analyze the performance of each model, Figure. A.15 illustrates the temporal variance of the reconstructed images from the SENSE, mSPECS, mSPECS-VAT, mSPECS-CAIPIRINHA, and mSPECS-CAIPIVAT models at different acceleration factors for slice 3. When comparing these four models, we observe a decreasing temporal variance from the SENSE model to the mSPECS-CAIPIVAT model at the same acceleration factor. As the acceleration factor increases, the temporal variance decreases for the mSPECS, mSPECS-VAT, mSPECS-CAIPIRINHA, and mSPECS-CAIPIVAT models, while it
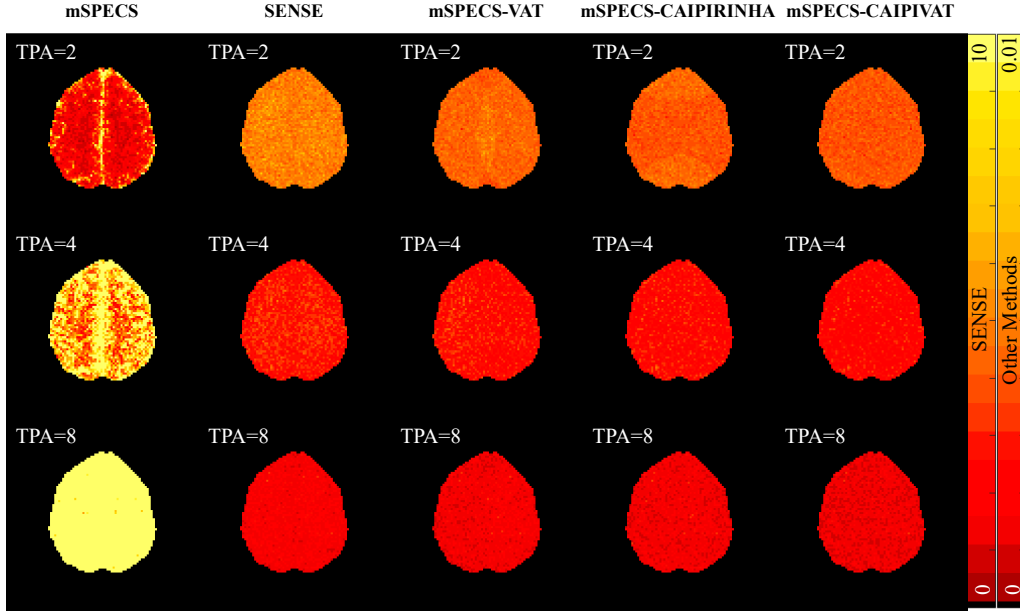
32

Figure A.15: The temporal variance of SENSE, mSPECS, mSPECS-VAT, mSPECS-CAIPIRINHA, and mSEPCS-CAIPIVAT model with different acceleration factors of slice 3.

increases for the SENSE model. Among the three mSPECS-based models, the mSPECS-CAIPIVAT model achieves the lowest temporal variance.

To evaluate and compare the changes in SNR and g-factor values for each tissue type across different methods and through-plane acceleration factors, Table A.1 presents the average SNR values for cerebral spinal fluid (CSF), gray matter (GM), and white matter (WM), as well as the average g-factor penalty for the whole brain. From Table A.1, we observe that the average SNR for CSF and GM in the standard SENSE model decreases slightly as the through-plane acceleration factor increases, while the average SNR for WM remains unchanged. In contrast, the average SNR for all tissue types in the other three models increases significantly with higher acceleration factors. Furthermore, the average g-factor for the SENSE model increases dramatically as the acceleration factor increases, compared to the modest increase in the average g-factor observed in the mSPECS, mSPECS-VAT, mSPECS-CAIPIRINHA, and mSPECS-CAIPIVAT models. Notably, compared to the mSPECS model, the three slice-wise image shift models, mSPECS-VAT, mSPECS-CAIPIRINHA and mSPECS-CAIPIVAT, exhibit

33

| | SENSE | | | |
Acceleration	CSF-SNR	GM-SNR	WM-SNR	g-factor
TPA=2	2.25	1.95	1.92	14.21
TPA=4	1.96	1.92	1.91	21.28
TPA=8	1.91	1.91	1.91	30.13
	mSPECS			
Acceleration	CSF-SNR	GM-SNR	WM-SNR	g-factor
TPA=2	55.00	19.06	12.11	1.30
TPA=4	73.49	25.29	16.11	1.39
TPA=8	101.14	34.92	22.20	1.44
	mSPECS-VAT			
Acceleration	CSF-SNR	GM-SNR	WM-SNR	g-factor
TPA=2	58.81	20.46	13.13	1.22
TPA=4	74.75	26.32	16.91	1.36
TPA=8	104.44	36.27	23.36	1.38
	mSPECS-CAIPIRINHA			
Acceleration	CSF-SNR	GM-SNR	WM-SNR	g-factor
TPA=2	59.85	21.13	13.54	1.16
TPA=4	76.25	26.87	17.38	1.27
TPA=8	104.98	36.82	23.69	1.34
	mSPECS-CAIPIVAT			
Acceleration	CSF-SNR	GM-SNR	WM-SNR	g-factor
TPA=2	61.11	21.41	13.73	1.15
TPA=4	78.19	27.56	17.89	1.27
TPA=8	107.72	37.97	24.50	1.29

Table A.1: The average SNR value for cerebrospinal fluid (CSF), gray matter (GM), and white matter (WM) with the average g-factor value of the whole brain with respect to SENSE, mSPECS, mSPECS-VAT, mSPECS-CAIPIRINHA, and mSPECS-CAIPIVAT methods with through-plane acceleration factors TPA=2, TPA=4, and TPA=8 for slice 3.

lower average g-factor penalties, with the mSPECS-CAIPIVAT model showing the lowest average g-factor.

Appendix A.2. Task Simulated Reconstruction Results

In Subsection. 3.3 of the main paper, we presented the *CNR* map for the SENSE, mSPECS, mSPECS-VAT, mSPECS-CAIPIRINHA, and mSPECS-
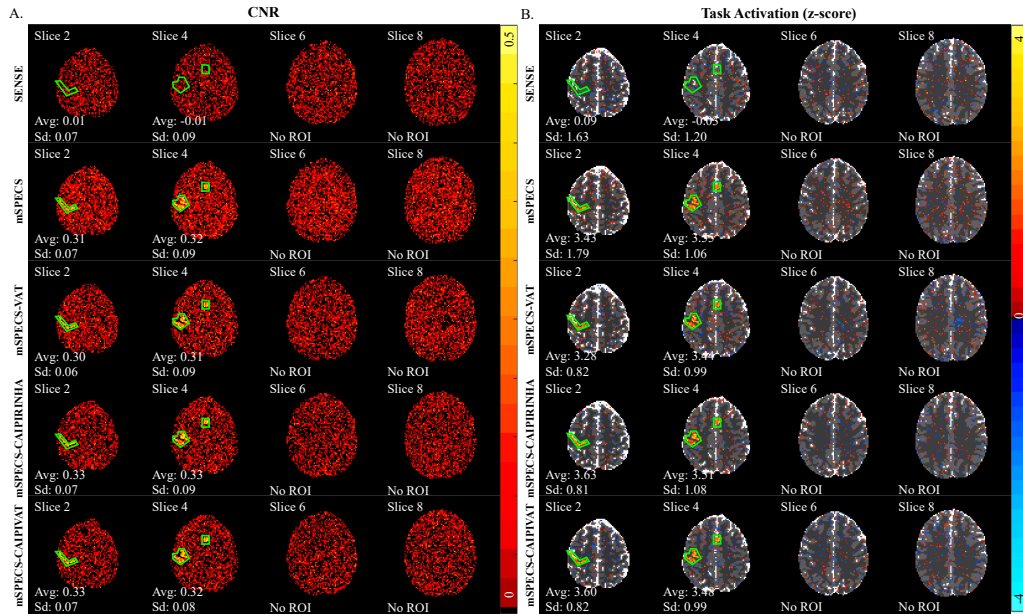
Figure A.16: A. The *CNR* map and the average *CNR* value and standard deviation of *CNR* of ROI for SENSE, mSPECS, mSPECS-VAT, mSPECS-CAIPIRINHA and mSPECS-CAIPIVAT model for even slices with TPA=2. B. The activation detection map and the average and standard deviation of z-score of ROI for SENSE, mSPECS, mSPECS-VAT, mSPECS-CAIPIRINHA and mSPECS-CAIPIVAT model for even slices with TPA=2.

CAIPIVAT models for odd slices at TPA=2, along with the average *CNR* value and standard deviation for the region of interest (ROI). Figure. A.16 displays the *CNR* maps and task activation maps for even slices for the SENSE, mSPECS, mSPECS-VAT, mSPECS-CAIPIRINHA, and mSPECS-CAIPIVAT models with an acceleration factor of TPA=2. Similar to the conclusion drawn in the main paper, the *CNR* maps and task activation maps show that the SENSE model struggles to capture the activation signal in the left-hand side motor cortex within the brain images. In contrast, the other three models effectively capture the clear simulated activation blocks. Additionally, the slice-wise image shift techniques yield a higher average z-score for the ROI compared to the mSPECS model. The mSPECS-CAIPIVAT model provides the highest average z-score for the ROI, indicating that it performs best in detecting activation signals.
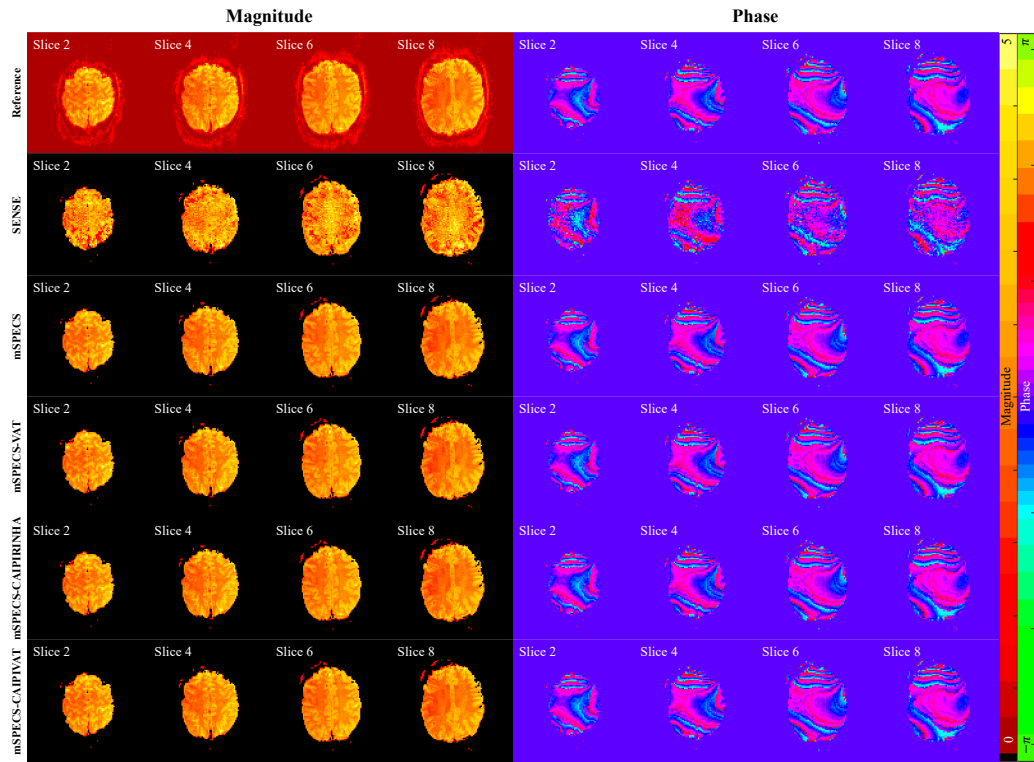
Figure A.17: The temporal mean magnitude and temporal mean phase of the axial brain images from the reference, SENSE, mSPECS, mSPECS-VAT, mSPECS-CAIPIRINHA, and mSPECS-CAIPIVAT for even slices with acceleration factor TPA=2.

Appendix A.3. Non-Task Experimental Reconstruction Results

In Subsection. 4.2 of the main paper, we display the temporal mean magnitude and mean phase of the reconstructed images from the reference, SENSE, mSPECS, mSPECS-VAT, mSPECS-CAIPIRINHA, and mSPECS-CAIPIVAT models for odd slices with an acceleration factor of TPA=2. Figure A.17 presents the temporal mean magnitude and mean phase of the even slices of axial brain images from the reference, SENSE, mSPECS, mSPECS-VAT, mSPECS-CAIPIRINHA, and mSPECS-CAIPIVAT models with TPA=2. Aliased artifacts from other slices are clearly visible in the magnitude and phase reconstructed brain images from the SENSE model, whereas the mean magnitude and mean phase from the mSPECS, mSPECS-VAT, mSPECS-CAIPIRINHA, and mSPECS-CAIPIVAT models are closely aligned with the reference magnitude and phase. From Figure. A.18, we
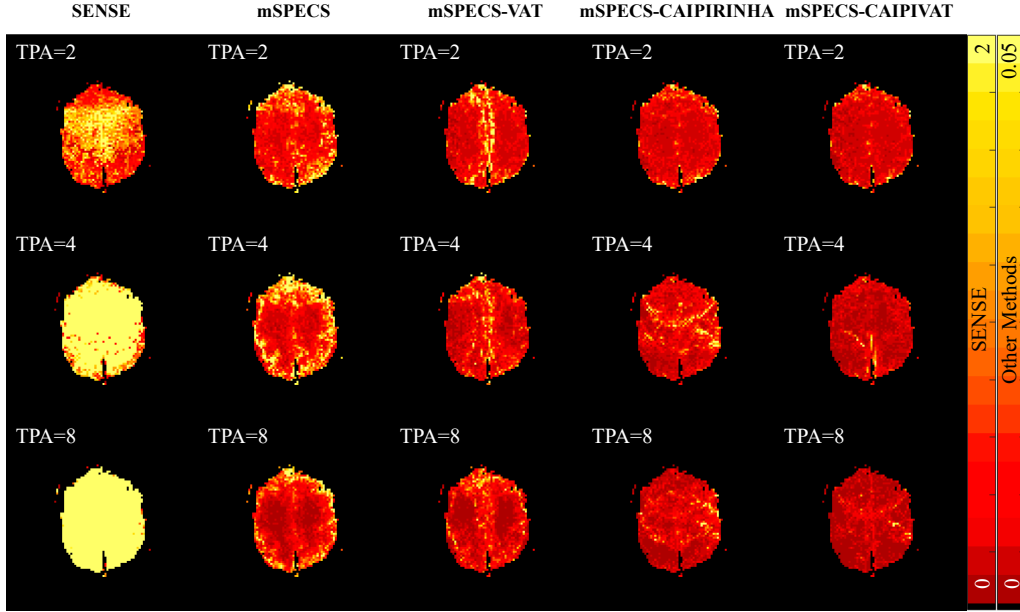
Figure A.18: The temporal variance of SENSE, mSPECS, mSPECS-VAT, mSPECS-CAIPIRINHA, and mSEPCS-CAIPIVAT model with different acceleration factors of slice 3.

observe that the temporal variance from the SENSE model increases with increasing acceleration factor, whereas the temporal variance from the mSPECS, mSPECS-VAT, mSPECS-CAIPIRINHA, and mSPECS-CAIPIVAT models decreases as the acceleration factor increases. Furthermore, when comparing the mSPECS model with the three slice-wise image shift techniques, the mSPECS-VAT, the mSPECS-CAIPIRINHA and mSPECS-CAIPIVAT models provide lower temporal variance, with the mSPECS-CAIPIVAT model yielding the lowest temporal variance results.

Appendix A.4. Task Experimental Reconstruction Results

Figure. A.19A shows the *CNR* value map for odd axial brain slices from the SENSE, mSPECS, mSPECS-VAT, mSPECS-CAIPIRINHA, and mSPECS-CAIPIVAT models with an acceleration factor of TPA=2. The average and standard deviation of the *CNR* values for the ROI are also shown in Figure. A.19A. From Figure. A.19A, it is evident that the SENSE model cannot detect any activation blocks in the right motor cortex brain area. In contrast, the other three models, mSPECS, mSPECS-VAT, mSPECS-

CAIPIRINHA, and mSPECS-CAIPIVAT can detect clear activation blocks with detailed anatomical structures. When comparing the average *CNR* values of the ROI, the three slice-wise image shift techniques, mSPECS-VAT, mSPECS-CAIPIRINHA and mSPECS-CAIPIVAT, have higher values than the mSPECS model. Figure. A.19B presents the activation block detection maps from the four models with an acceleration factor of TPA=2. The average and standard deviation of the z-scores for the ROI are also shown in Figure. A.19B. Similar to the *CNR* maps, the SENSE model fails to detect any activation blocks within the brain. The mSPECS, mSPECS-VAT, mSPECS-CAIPIRINHA, and mSPECS-CAIPIVAT models capture the activation signals with clear shapes and anatomical structures. The average z-score of the ROI from the two slice-wise image shift techniques is higher than that of the mSPECS model, with the mSPECS-CAIPIVAT model providing the highest average z-score for the ROI. A similar conclusion can be drawn from the *CNR* maps and task activation detection maps for even slices of the experimental reconstructed images.

References

Barth, M., Breuer, F., Koopmans, P. J., Norris, D. G., and Poser, B. A. *Simultaneous multislice (SMS) imaging techniques*, Magn Reson Med, 75(1):63–81.

Breuer, F. A., Blaimer, M., Heidemann, R. M., Mueller, M. F., Griswold, M. A., and Jakob, P. M. *Controlled aliasing in parallel imaging results in higher acceleration (CAIPIRINHA) for multi-slice imaging*, Magn Reson Med, 53(3):684–91.

Feinberg, D. A., Hale, J. D., Watts, J. C., Kaufman, L., and Mark, A. *Halving MR imaging time by conjugation: demonstration at 3.5 kG*, Radiology, 161(2), 527-531.

Glover, G. H. *Overview of functional magnetic resonance imaging*, Neurosurg Clin N Am, 22(2):133–9, vii.

Griswold, M. A., Jamob, P. M., Heidemann, R. M., Nikkka, M., Jellus, V., Wang, J., Kiefer, B., and Haase, A. *Generalized autocalibrating partially parallel acquisition (GRAPPA)*, Magn Reson Med, 47:1202–1210.
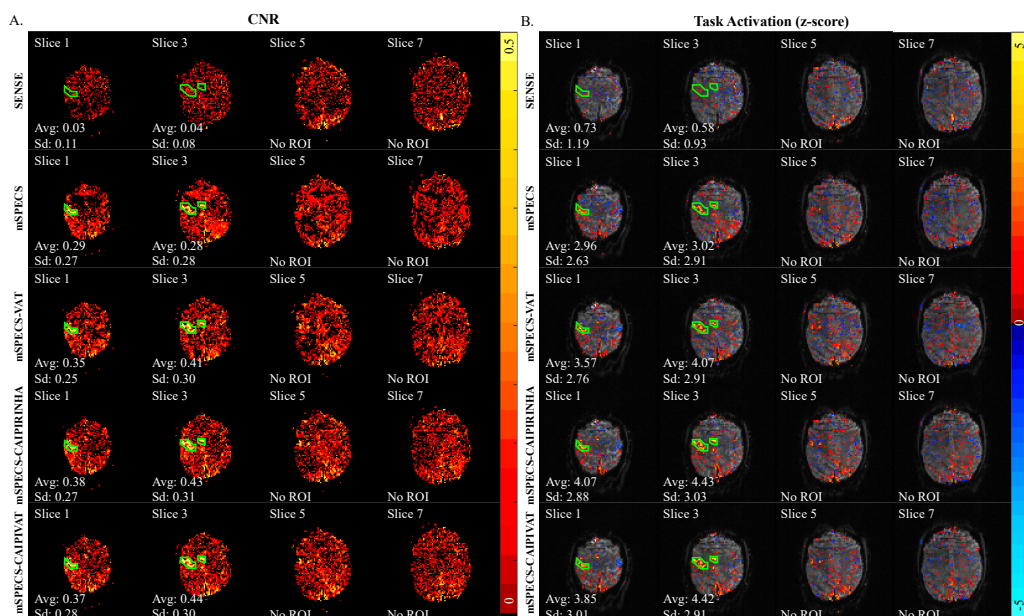
Figure A.19: A. The *CNR* map and the average *CNR* value and standard deviation of *CNR* of ROI for SENSE, mSPECS, mSPECS-CAIPIRINHA and mSPECS-CAIPIVAT model for odd slices with TPA=2. B. The activation detection map and the average and standard deviation of z-score of ROI for SENSE, mSPECS, mSPECS-CAIPIRINHA and mSPECS-CAIPIVAT model for odd slices with TPA=2.

Hyde, J. S., Jesmanowicz, A., Froncisz, W., Kneeland, J. B., Grist, T. M., and Campagna, N. F. *Parallel image acquisition from noninteracting local coils*, Journal of Magnetic Resonance, 70(3), 512-517.

Jungmann, P. M., Ganter, C., Schaeffeler, C. J., Bauer, J. S., Baum, T., Meier, R., and Woertler, K. *View-Angle Tilting and Slice-Encoding Metal Artifact Correction for Artifact Reduction in MRI: Experimental Sequence Optimization for Orthopaedic Tumor Endoprostheses and Clinical Application*, PLoS One, 10(4):e0124922.

Kociuba, C. M. *A Fourier description of covariance, and separation of simultaneously encoded slices with in-plane acceleration in fMRI*, Ph.D. Dissertation, Marquette University, Milwaukee, Wisconsin, USA.

Kornak, J., Young, K., Schuff, N., Du, A., Maudsley, A. A., and Weiner, M.

W. *K-Bayes reconstruction for perfusion MRI I: Concepts and application*, Journal of digital imaging, 23, 277-286.

Lindquist, M. A., Zhang, C. H., Glover, G., and Shepp, L. *Rapid three-dimensional functional magnetic resonance imaging of the initial negative BOLD response*, Journal of Magnetic Resonance, 191(1), 100-111.

Mansfield P. *Multi-planar image formation using NMR spin echoes[J]*, Journal of Physics C: Solid State Physics, 10(3): L55.

Min-Oh Kim, Taehwa Hong, and Dong-Hyun Kim. *Multislice CAIPIRINHA Using View Angle Tilting Technique (CAIPIVAT)*, Tomography, 43-48.

Min-Oh Kim, Sang-Young Zho, and Dong-Hyun Kim. *3D imaging using magnetic resonanace tomosynthesis (MRT) technique*, Med. Phys, 39(8): 4733-4741.

Nencka, A. S., Shefchik, D. L., Huettner, A. M., and Jesmanowicz A. *Auto-Calibrated Multiband Imaging with Phase Tagging and Hadamard Encoding*, ISMRM Workshop on Data Sampling and Image Reconstruction, Sedona, AZ, 2013, 16.

Nencka, A. S. and Jesmanowicz A. *Moving Window Auto-Calibrated Multiband Imaging for Minimized Residual Correlation*, ISMRM Workshop on Data Sampling and Image Reconstruction, Sedona, AZ, 2013, 11.

Noll, D. C., Nishimura, D. G., and Macovski, A. *Detection in magnetic resonance imaging*, IEEE transactions on medical imaging, 10(2), 154-163.

Ogawa, S., Lee, T. M., Kay, A. R., and Tank, D. W. *Brain magnetic resonance imaging with contrast dependent on blood oxygenation*, Proc Natl Acad Sci USA, 87(24):9868-721.

Poustchi-Amin, M., Mirowitz, S. A., Brown, J. J., Mcinstry, R. C., and Li, T. *Principles and Applications of Echo-Planar Imaging: A Review for the General Radiologist*, RadioGraphics, 21:3, 767-779.

Preibisch, C., Castrillón G., J. G., Bührer, M., and Riedl, V. *Evaluation of Multiband EPI Acquisitions for Resting State fMRI*, PLoS ONE, 10(9): e0136961.

Pruessmann, K. P., Weiger, M., Scheidegger, M. B., and Boesiger, P. *SENSE: Sensitivity Encoding for Fast MRI*, Magn Reson Med, 42:952–962.

Rzedzian, R., Mansfield, P., Doyle, M., Guilfoyle, D., Chapman, B., Coupland, R. E., Chrispin, A., and Small, P. *Real-time nuclear magnetic resonance clinical imaging in pediatrics*, The Lancet, 322:1281-2.

Risk, B. B., Murden, R. J., Wu, J., Nebel, M. B., Venkataraman, A., Zhang, Z., and Qiu, D. *Which multiband factor should you choose for your resting-state fMRI study?*, Neuroimage, 234:117965.

Rowe, D. B., Bruce, I. P., Nencka, A. S., Hyde, J. S., and Kociuba, M. C. *Separation of parallel encoded complex-valued slices (SPECS) from a signal complex-valued aliased coil image*, Magn Reson Imaging, 34(3):359-69.

Rowe, D. B., and Logan, B. R. *A complex way to compute fMRI activation*, Neuroimage, 23(3):1078-92.

Rowe, D. B., Nencka, A. S., Jesmanowicz, A., and Hyde, J. S. *Separation of two simultaneously encoded slices with a single coil*, In Proc Intl Soc Magn Reson Med, Vol. 21, p. 0123.

Setsompop, K., Gagoski, B. A., Polimeni, J. R., Witzel, T., Wedeen, V. J., and Wald, L. L. *Blipped-controlled aliasing in parallel imaging (blipped-CAIPI) for simultaneous multi-slice EPI with reduced g-factor penalty*, Magn Reson Med, 67(5): 1210-1224.

Souza, S. P., Szumowskim, J., Dumoulin, C. L., Plewes, D. P., and Glover, G. *SIMA - simultaneous multislice acquisition of MR images by Hadamard-encoded excitation*, J Comput Assist Tomogr, 12:1026–1030.

Welvaert, M. and Rosseel, Y. *On the Definition of Signal-To-Noise Ratio and Contrast-To-Noise Ratio for fMRI Data*, J PloS ONE, 8(11): e77089.